UNIVERSITATEA BABEȘ-BOLYAI
BABEȘ-BOLYAI TUDOMÁNYEGYETEM
BABEȘ-BOLYAI UNIVERSITÄT
BABEȘ-BOLYAI UNIVERSITY
TRADITIO ET EXCELLENTIA

BABEȘ-BOLYAI UNIVERSITY

Faculty of Chemistry and Chemical Engineering

PhD Thesis Summary

From molecular inorganic species to organometallic nanoparticles: a DFT journey

Scientific advisor:

Prof. Dr. Luminița Silaghi-Dumitrescu

PhD candidate:

Ionuț-Tudor Moraru

Cluj-Napoca

2022

Jury

President:

Prof. Dr. Gabriela Nicoleta Nemeș, Babeș-Bolyai University, Cluj-Napoca, Romania

Scientific advisor:

Prof. Dr. Luminița Silaghi-Dumitrescu, Babeș-Bolyai University, Cluj-Napoca, Romania

Reviewers:

Prof. Dr. Romuald Poteau, Université Paul Sabatier, Toulouse, France

Prof. Dr. Aurel Pui, Alexandru Ioan Cuza University, Iași, Romania

Prof. Dr. Vasile Chiș, Babeș-Bolyai University, Cluj-Napoca, Romania

Contents of the PhD Thesis

Keywords: inorganic amines/ethers; attraction-repulsion offsets; ultra-small RuNPs; surface carbides; ancillary ligands; HDMS-decorated NP; DFT calculations

Contents of the Summary

General Introduction

The thesis project represents an extensive density functional theory (DFT) study, which explores a wide range of systems, from molecular species to transition-metal nanoclusters, being divided into three main parts.

The first topic is related to molecular chemistry and represents a fundamental research of the nature of E-O and E-N chemical bonds (E = C, Si, Ge, Sn). A large number of model compounds are investigated, such as hydrogenated, methylated or halogenated ether-like systems, short-chain acyclic oligomers incorporating the E-O-E motif, cationic oxonium species and amine-like derivatives (referred in the thesis as inorganic ethers and inorganic amines). The study accounts for both organic and heavier inorganic counterparts. The aim was to develop a general bonding mechanism that fits all of these species.

The second topic addresses the carbide formation issue in the context of the CO hydrogenation process catalyzed by ultra-small ruthenium nanoparticles (Ru NPs). The study involves complex mechanistic investigations on realistic NP models, to evaluate the thermodynamic and kinetic accessibility of the ruthenium surface carbides, as well as DFT-NMR calculations to secure experimental spectroscopic data assignment. This subject was developed at Université Paul Sabatier, Toulouse, in the group of Prof. Romuald Poteau.

The last part of the thesis combines the knowledge gathered in the first two chapters. This closing chapter aims at designing new nanoscale catalysts, *i.e.* ultra-small RuNPs decorated with silylamine ligands, by blending the special electronic features of inorganic molecules, such as heavier amine counterparts, with the surface properties of ruthenium nanoclusters.

Chapter 1

Investigations into the nature of the chemical bonding of organic and inorganic ethers & amines

1.1 Introduction and Literature Data

The present chapter concerns a theoretical study of species containing E-O-E and E_3N fragments (E = C, Si, Ge, Sn), and brings insights into their chemical bonding. Inorganic counterparts of both amines and ethers exhibit an increased chemical inertness compared to organic derivatives.[1-3] According to literature data,[4,5] such contrasting properties originate in the complex bonding phenomena occurring within the inorganic species, while the chemical bonding of Si-O-Si moieties was regarded as "elusive".[6]

The molecular chemistry of inorganic $(R_3E)_2O$ and $(R_3E)_3N$ derivatives has shown interest to the scientific community from both theoretical[4,5,7-22] and experimental[1,2,23-30] viewpoints. Among these derivatives, siloxanes, *i.e.* compounds incorporating Si-O-Si units, are famous for their various practical applications.

The complex secondary electronic phenomena occurring at the level of E-O and E-N bonds (E = heavier Group 14 element) are strongly reflected in the equilibrium molecular geometries of inorganic amines and ethers.[9-12,22,30] But probably the most intriguing aspect for the theoretical chemistry community is the structural contrast between organic amines/ethers and their heavier inorganic counterparts, discrepancies that were highlighted in various papers.[4,5,17,19]

A concept widely used to explain the peculiar structural features of heavier ether/amine counterparts and accounts for departures from the essential covalent image of main group derivatives, is that of hyperconjugation[31-34]. Historically speaking, hyperconjugation superseded

bonding models based on p→d back-donations and has gained notoriety in the last three decades (hyperconjugative and p→d effects are schematically illustrated in ***Figure 1.1***).

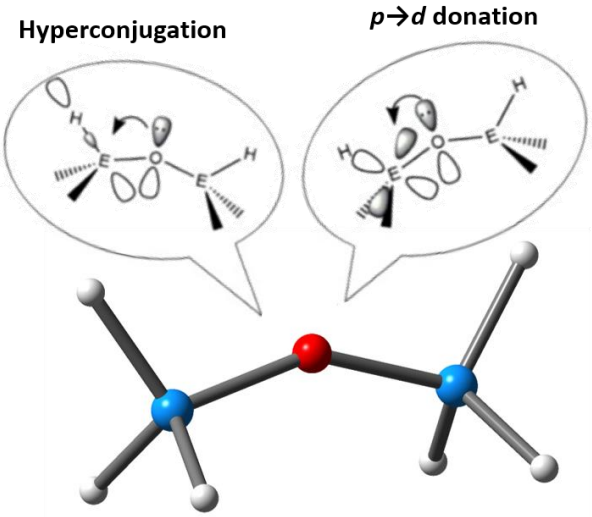

Figure 1.1. Schematic illustration of vicinal LP(O)→σ*(Si-H) hyperconjugative interactions and of p(O)→d(Si) donations occurring within Si-O-Si units.

The nature of the Si-O bond has been the central subject of numerous works, but owing to conflicting opinions, further explanations are needed. For germoxanes and stannoxanes theoretical studies regarding their bonding are few, although the structural features of Ge-O-Ge and Sn-O-Sn fragments reproduce to some extent the ones of Si-O-Si units. For the inorganic counterparts of amines, bonding investigations are as well significantly fewer compared to those on siloxanes. Therefore, clarifications regarding the physical mechanism of E-O and E-N bonds (E = C, Si, Ge, Sn) are required.

1.2 Original contributions

Theoretical calculations are carried out on a wide range of model compounds containing E-O or E-N bonds (E = C, Si, Ge, Sn), to bring further clarifications on their bonding mechanism. For these purposes, the following E-O-E systems are studies: $(R_3E)_2O$, $(R_3E)OH$, $(XH_2E)_2O$, $(X_2HE)_2O$ derivatives (R= H or Me; X = F or Cl), acyclic oligomers incorporating E-O-E units, $[(R_3E)_3O]^+$ oxonium. Regarding amines, both organic and inorganic counterparts of $(R_3E)_3N$, $(R_3E)_2NH$ and $(R_3E)NH_2$ derivatives are assessed.

Organic *vs.* Inorganic Hydrogenated and Methylated Ethers

The general structures of investigated $(R_3E)_2O$ systems are illustrated in ***Scheme 1.1***.

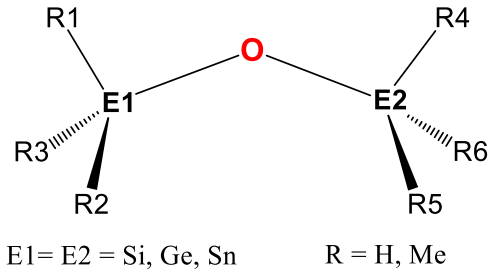

Scheme 1.1. Schematic representation of model $(R_3E)_2O$ derivatives investigated throughout this study

The molecular geometries of these species are optimized at the DFT level of theory, by employing the triple-zeta quality Def2-TZVP basis set and the PBE0 hybrid functional. Equilibrium E-O-E angles and E-O bond lengths (*i.e.* the structural parameters of interest for the current purposes) are close to the experimental measured values (***Table 1.1***), stressing that PBE0/Def2-TZVP DFT level represents a good choice for investigating the molecular features of derivatives incorporating the E-O-E fragment.

Table 1.1. DFT (**PBE0/Def2-TZVP**) computed values of the E-O-E angles and E-O bond distances of investigated model ethers (the calculated bond lengths of E1-O and O-E2 bonds depicted in ***Scheme 1.1*** are equivalent); experimental values are displayed for comparisons (experimental measurements were obtained by electron diffraction in gaseous phase). Computed bond orders for the E-O bonds are displayed. The expected E-O lengths are obtained by summing the individual covalent radii of E and O atoms.

E	R	E-O-E (°)		E-O (Å)			
		PBE0	**measured**	**PBE0**	**Measured**	**Σ*cov*(E+O) [*ref. 35*]**	**NRT bond order**
C	H	**112.1**	111.8[36]	**1.399**	1.415[36]	*1.42*	**1.07**
	Me	**127.1**	130.8[37]	**1.429**	1.420[37]		**0.97**
Si	H	**148.7**	144.1[38,39]	**1.634**	1.634[38,39]	*1.77*	**1.16**
	Me	**150.9**	148.0[38]	**1.641**	1.631[38]		**1.19**
Ge	H	**128.1**	126.5[40]	**1.779**	1.766[40]	*1.86*	**1.10**
	Me	**134.0**	141.0[41]	**1.780**	1.770[41]		**1.15**
Sn	H	**133.5**	–	**1.954**	–	*2.05*	**1.15**
	Me	**135.1**	140.8[41]	**1.962**	1.940[41]		**1.13**

According to the equilibrium geometries of $(R_3E)_2O$ species, the E-O-E angles of heavier ethers are considerably wider than the C-O-C ones of organic ones. In addition, the E-O bond distances of inorganic derivatives are significantly shorter than expected values (*i.e.* reference values are obtained by summing the covalent radii of E and O atoms), while the C-O bond distances of organic ethers are not (***Table 1.1***).

The potentials to linearization of the E-O-E units are also evaluated for all model $(R_3E)_2O$ (E = C, Si, Ge, Sn) systems (***Table 1.2***). It is shown that organic ethers display high linearization potentials, while for the inorganic derivatives these are much lower.

Table 1.2. Calculated linearization potentials for model $(R_3E)_2O$ systems.

	E	PBE0/Def2-TZVP			
		C	**Si**	**Ge**	**Sn**
R	H	34.0	0.3	3.6	2.0
	Me	22.5	0.2	3.4	2.5

Natural bond orbital (NBO) calculations are carried out on the equilibrium structures of investigated E-O-E systems, in order to gain insights into their secondary electronic properties. Among the donor-acceptor interactions determined, special attention is paid to vicinal hyperconjugations, type LP(O)→σ*(E-R) (E = C, Si, Ge, Sn; R = H, Me) (***Figure 1.2***). These donor-acceptor interactions originate in two different lone pair of electrons (LPs): one exhibits a mixed s/p atomic orbital character, while the other is a pure p atomic orbital.

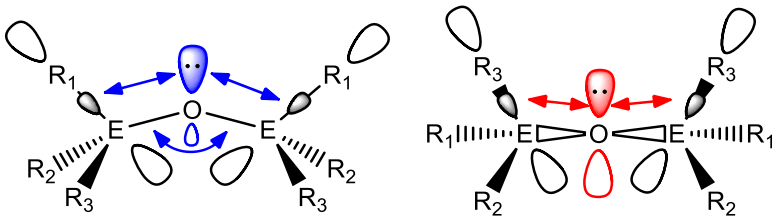

Figure 1.2. Schematic representation of the $LP_1(O)$→σ*(E-R) (*left side*) and $LP_2(O)$→σ*(E-R) (*right side*) hyperconjugations occurring within E-O-E moieties (E = C, Si, Ge, Sn).

Orbital overlaps corresponding to the highest energy hyperconjugation interactions, originating in both LPs, are illustrated in ***Figure 1.3***, as a particular case of hydrogenated ethers. Fully methylated counterparts reveal similar interactions. In addition to the depicted interactions, other lower energy hyperconjugations occur in the E-O-E unit. In fact, the total hyperconjugation energy per E-O-E unit (*i.e.* summation of all individual interaction energies) is a parameter of interest for the current purposes (***Table 1.3***).

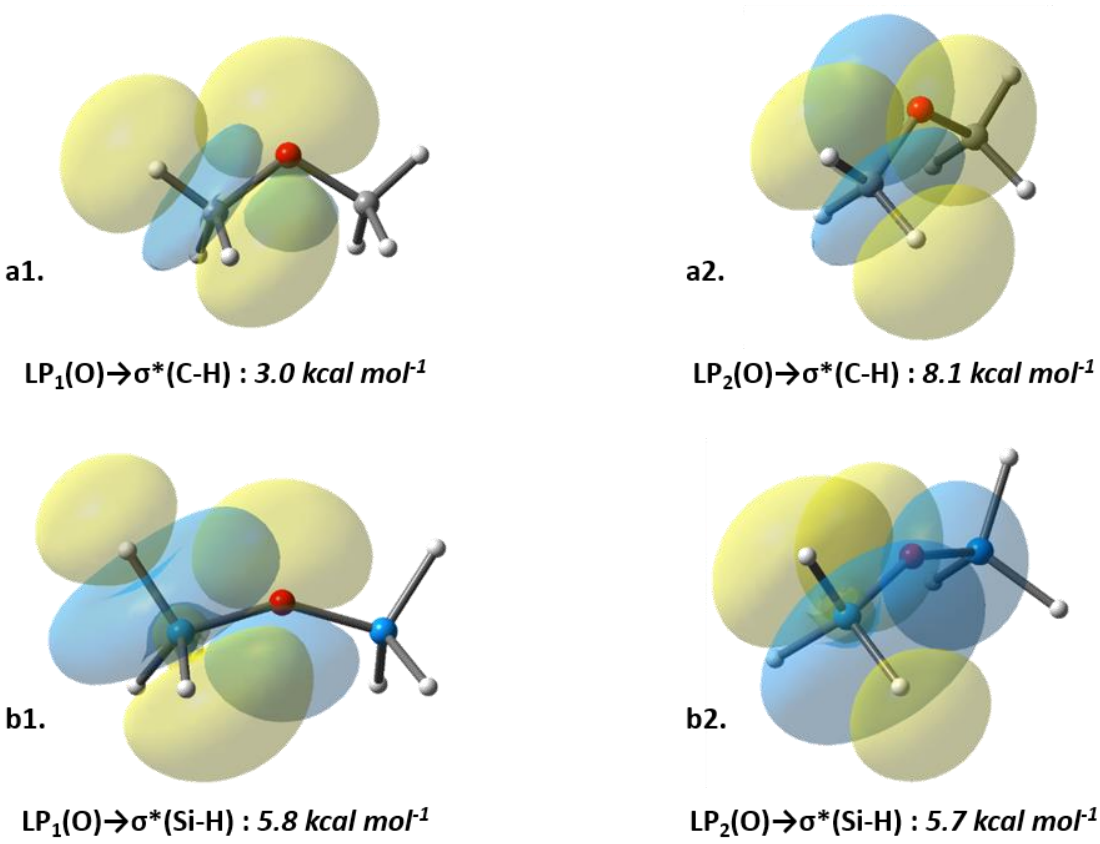

Figure 1.3. Highest-energy vicinal hyperconjugative interactions, of LP(O)→σ*(E-H) general type, occurring within the E-O bonds of the following molecules:

Me_2O: **a1)** $LP_1(O)\rightarrow\sigma^*(C\text{-}H)$; **a2)** $LP_1(O)\rightarrow\sigma^*(C\text{-}H)$

$(H_3Si)_2O$: **b1)** $LP_1(O)\rightarrow\sigma^*(Si\text{-}H)$; **b2)** $LP_1(O)\rightarrow\sigma^*(Si\text{-}H)$

*for the *$(H_3Ge)_2O$* and *$(H_3Sn)_2O$* derivatives, similar orbital overlaps were observed

Table 1.3. Total hyperconjugation energy (PBE0/Def2-TZVP) per E-O-E unit (*i.e.* amounting all hyperconjugative effects originating in $LP_1(O)$ and $LP_2(O)$ orbitals).

E	R	C	Si	Ge	Sn
Σ [$LP_1(O)\rightarrow\sigma^*(E\text{-}R)$ + $LP_2(O)\rightarrow\sigma^*(E\text{-}R)$] (kcal/mol)	H	41.6	39.8	27.0	18.4
	Me	43.2	46.8	31.4	21.2

Additional to the vicinal hyperconjugations, LP(O)→d(E) (E = Si, Ge Sn) donations display significant contributions to the secondary electronic effects, within all heavier homologues of ethers (***Table 1.4***). Still, their energies are lower than those of corresponding the LP(O)→σ*(E-H) effects.

Table 1.4. Total p→d donation energy (PBE0/Def2-TZVP) per E-O-E unit (*i.e.* amounting all LP(O)→d(E) effects originating in LP_1(O) and LP_2(O) orbitals).

E	R	C	Si	Ge	Sn
Σ [LP_1(O)→d(E) + LP_2(O)→d(E)] (kcal/mol)	H	-	19.2	9.6	6.4
	Me	-	14.4	7.6	7.8

The total attraction energy per E-O-E unit, obtained by summing the energies of all LP(O)→σ*(E-H) and LP(O)→d(E) interactions, is also evaluated (***Table 1.5***). Regarding organic ethers, the total attraction energy coincides with the hyperconjugation energy.

Table 1.5. Total attraction energy (PBE0/Def2-TZVP) per E-O-E unit (*i.e.* the sum of hyperconjugation and p→d donation energies).

E	R	C	Si	Ge	Sn
Σ [LP_1(O)→σ*(E-R) + LP_2(O)→σ*(E-R) + LP_1(O)→d(E) + LP_2(O)→d(E)] (kcal/mol)	H	41.6	59.0	36.6	24.8
	Me	43.2	61.2	39.0	29.0

Natural bond orbital deletion (NBO DEL) calculations are carried out on the investigated model E-O-E systems, in order to understand the manner in which LP(O)→σ*(E-R) and LP(O)→d(E) interactions affect their equilibrium properties. Thus, optimizations carried out in absence of all LP(O)→d(E) and LP(O)→σ*(E-H) effects lead for all inorganic derivatives to E-O-E (E = Si, Ge, Sn) angles that are close to 111.5°, reference value representing the widening of equilibrium C-O-C angles of organic ethers. At the same time, the E-O bond distances of all inorganic $(H_3E)_2O$ species are considerably elongated with respect to their equilibrium length. These E-O bonds exhibit, following the deletion of hypeconjugations and p→d effects, distances

that are comparable to their covalent radii (***Table 1.6***). In addition, comparisons with the NBO DEL optimizations carried out in the absence of hyperconjugations only, emphasize that LP(O)→d(E) donations gave certain influence on the geometries of inorganic E-O-E systems, despite the common belief that they are merely computational artefacts originating in the polarization functions of the basis sets.

Table 1.6. NBO DEL values of the E-O-E angles and E-O bond lengths obtained in the absence of all $LP_1(O)\rightarrow\sigma^*(E\text{-}H)$ and $LP_2(O)\rightarrow\sigma^*(E\text{-}H)$ hyperconjugations, and of $LP_1(O)\rightarrow d(E)$ and $LP_2(O)\rightarrow d(E)$ donations occurring within model $(H_3E)_2O$ ethers. Equilibrium E-O-E and E-O values are presented, for comparisons. Calculated gaps between NBO DEL values and the equilibrium geometry ones are as well shown, along with expected E-O bond distances obtained by covalent radii summation.

E	**R**	**NBO DEL optimizations**		**Equilibrium Geom.**		***Δ (NBO DEL – Eq. Geom.)***		**Σ*cov*(E+O)**
		E-O-E (°)	**E-O (Å)**	**E-O-E (°)**	**E-O (Å)**	**Δ E-O-E (°)**	**Δ E-O (Å)**	**(Å)**
Si	H	111.9	1.800	147.7	1.634	**-36.2**	**0.126**	*1.77*
Ge	H	113.7	1.874	127.8	1.774	**-13.9**	**0.073**	*1.86*
Sn	H	117.1	2.037	132.5	1.956	**-12.7**	**0.065**	*2.05*

Aside from impacting the widening of inorganic E-O-E units and their E-O bond distances, LP(O)→d(E) and LP(O)→σ*(E-H) interactions also affect the equilibrium conformations of $(H_3E)_2O$ model species. In fact, in the absence of all these secondary effects, conformations are drastically changed, ranging from eclipsed to staggered (***Figure 1.4***).

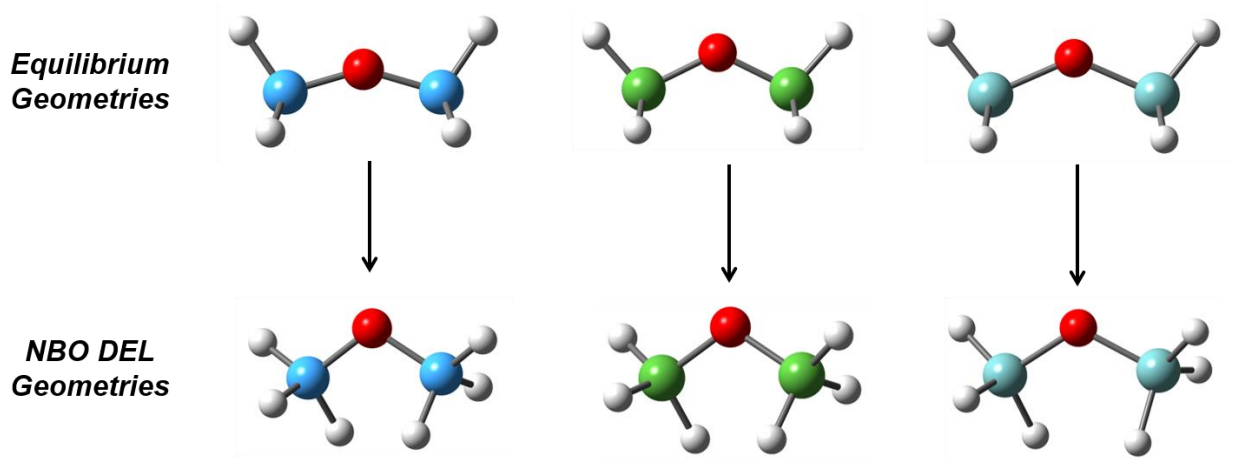

Figure 1.4. Structural changes occurring upon the removal at the E-O-E level of vicinal hyperconjugative interactions and p→d donations for disiloxane (*left*), digermoxane (*center*) and distannoxane (*right*) molecules.

Thus far, the structural features of heavier ether counterparts can be attributed to LP(O)→σ*(E-R) hyperconjugations and LP(O)→d(E) donations. Yet, equivalent electronic interactions barely affect the geometries of organic ethers, despite higher energies. Therefore, the structural contrast among organic and inorganic ethers cannot be justified solely because of such attractive effects, as previously suggested in literature. But the different structural behaviour of organic and inorganic counterparts can be motivated if vicinal Pauli repulsions, occurring between the lone pair electrons at the oxygen atom and the vicinal σ(E-R) bonds (***Figure 1.5***) are taken into account in addition to hyperconjugations. Their calculated energies are presented in ***Table 1.7***. Nevertheless, the driving force that dictates structural features of both organic and inorganic E-O-E systems is the counterbalance between attractions and repulsions.

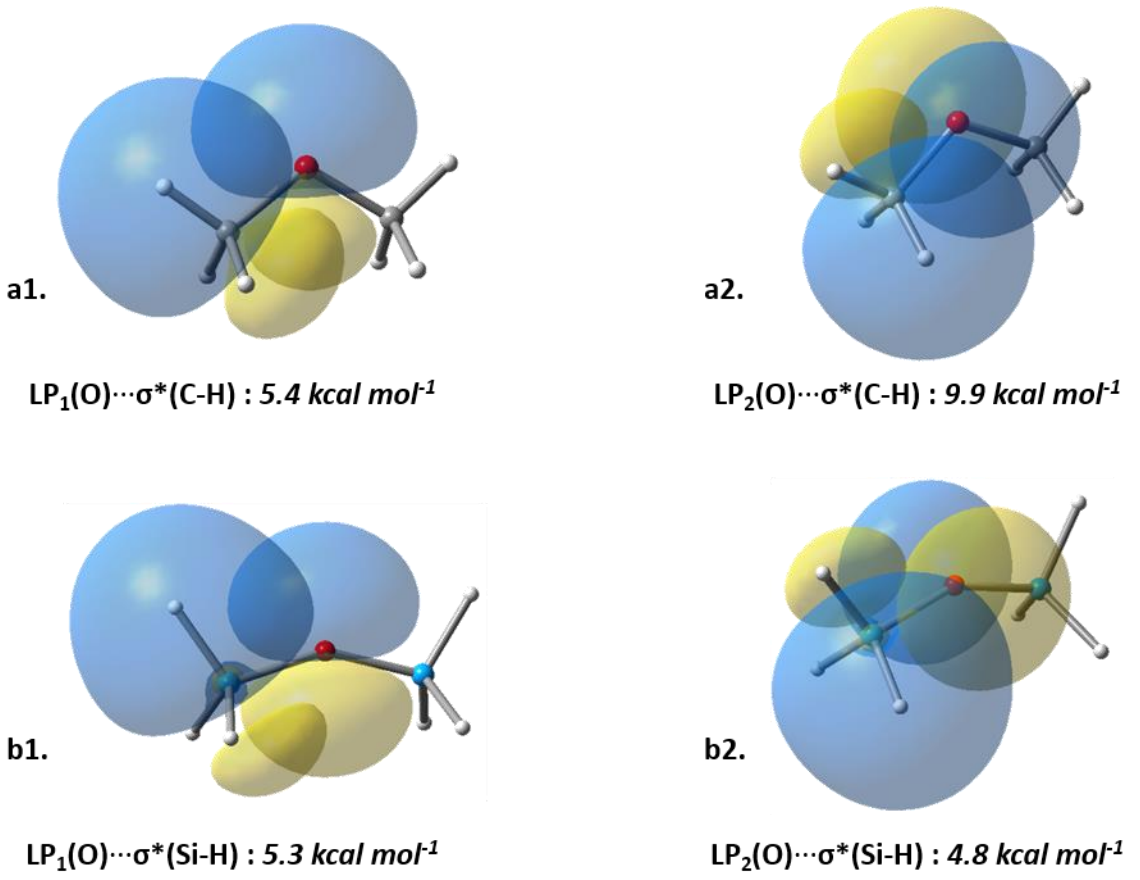

Figure 1.5. Highest-energy vicinal Pauli repulsions, of the LP(O)···σ*(E-H) general type, occurring within the E-O bonds of the following molecules:

Me_2O: **a1)** $LP_1(O)\cdots\sigma^*(C\text{-}H)$; **a2)** $LP_1(O)\rightarrow\sigma^*(C\text{-}H)$

$(H_3Si)_2O$: **b1)** $LP_1(O)\cdots\sigma^*(Si\text{-}H)$; **b2)** $LP_1(O)\rightarrow\sigma^*(Si\text{-}H)$

*for the *$(H_3Ge)_2O$* and *$(H_3Sn)_2O$* molecules, similar repulsive effects were observed

Attraction-repulsion offset (***Table 1.7***), *i.e.* energy differences between LP(O)→σ*(E-R), LP(O)→d(E) and LP(O)···σ(E−R) interactions, can motivate the different geometries of organic and inorganic counterparts, as follows: for organic ethers, repulsions overcome attractions, thus preventing the influence of the latter on the features of C-O-C fragments, while inorganic counterparts reveal the opposite. The current approach, based on offsets between vicinal

attractions and repulsions, represents a novel bonding model that has not been previously reported.

Table 1.7. Computed attraction, *i.e.* ∑LP(O)→σ*(E-R) + LP(O)→d(E), and repulsion, *i.e.* ∑ LP(O)···σ(E-R), energies per E-O bond. Offset values were determined as energy differences between attractions and repulsions are also displayed.

E	R	∑LP(O)→σ*(E-R) (kcal mol^{-1})	∑LP(O)→d(E) (kcal mol^{-1})	∑LP(O)→σ*(E-R) + LP(O)→d(E) (kcal mol^{-1})	∑ LP(O)···σ(E-R) (kcal mol^{-1})	ΔE (attraction-repulsion) (kcal mol^{-1})
C	H	19.6	–	**19.6**	**27.3**	**-7.7**
	Me	17.9	–	**17.9**	**27.3**	**-9.4**
Si	H	19.5	9.6	**29.1**	**14.9**	**14.2**
	Me	22.1	7.6	**29.6**	**13.7**	**16.0**
Ge	H	14.5	5.1	**19.5**	**11.3**	**8.2**
	Me	16.1	3.0	**19.1**	**10.2**	**8.9**
Sn	H	9.9	3.8	**13.7**	**6.8**	**6.9**
	Me	10.8	4.0	**14.8**	**6.4**	**8.4**

Angle-scanning calculations are further performed on the series of $(R_3E)_2O$ model derivatives (E = C, Si, Ge, Sn; R= H or Me). For both hydrogenated and methylated models, it is shown that attraction-repulsion offsets increase for all inorganic E-O-E units (E =Si, Ge, Sn) as the angle widens, in the same way as that the relative molecular energy decreases (***Figure 1.6***). But the opposite is illustrated for the organic counterparts. Therefore, maximization of the attraction-repulsion counterbalance on the investigated range explains the preference of inorganic species to adopt large E-O-E angles, while the constant positive value of such offsets motivates the short E-O bond distances of these heavier analogues of ethers.

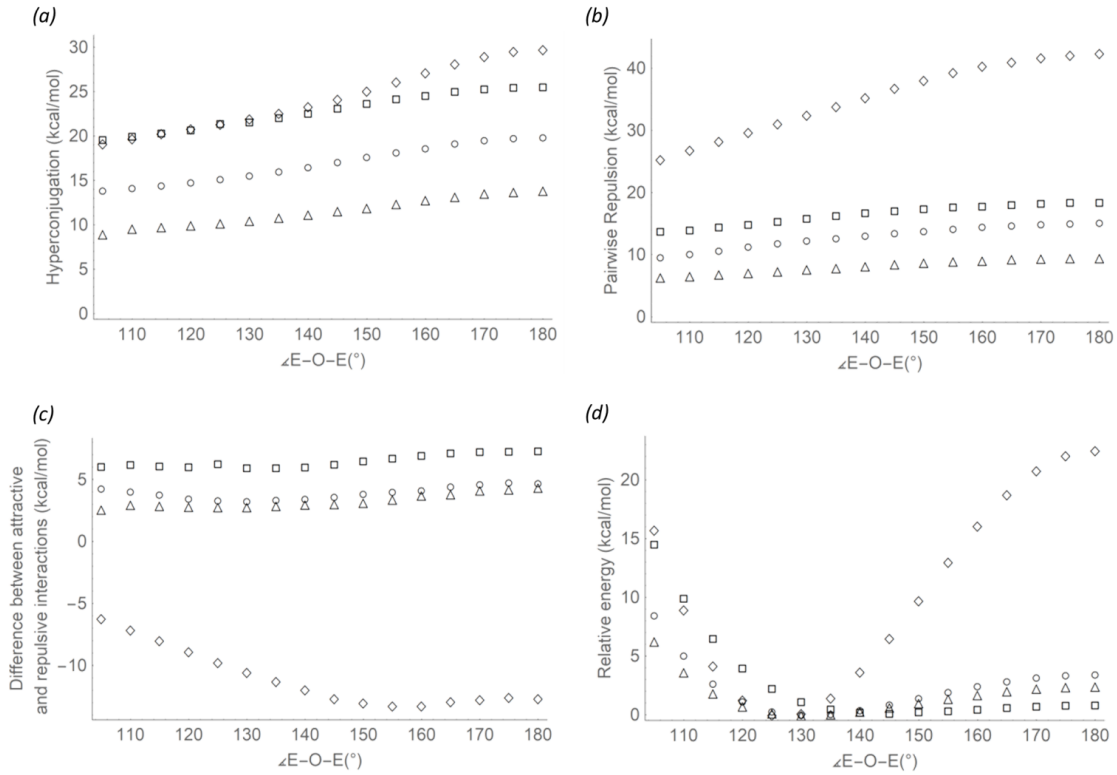

Figure 1.6. Calculated E-O-E dependence of several parameters: (a) total attraction energy; (b) total Pauli repulsion energy; (c) attraction-repulsion offset energy; (d) molecular energy, for model $(Me_3E)_2O$ derivatives (E = C – ◇, Si – □, Ge – ○, and Sn – △). Similar trends were obtained for $(H_3E)_2O$ counterparts (these illustrated in the main thesis manuscript).

Next, it is shown that the two different LP electrons at the oxygen atom of the E-O-E fragments, affect the equilibrium geometries in different manners. Based on attraction-repulsion offsets calculated separately for $LP_1(O)$ and $LP_2(O)$ (***Figure 1.7***), the following conclusions are drawn: the mixed s/p lone pair is mainly responsible for the bending behaviour of E-O-E units, *e.g.* dictates the wide angles of inorganic derivatives, while the pure p lone pair is responsible for the short E-O bond lengths of inorganic counterparts, although the s/p LP also has some minor impact on these bond distances. These observations are further confirmed by NBO DEL calculations.

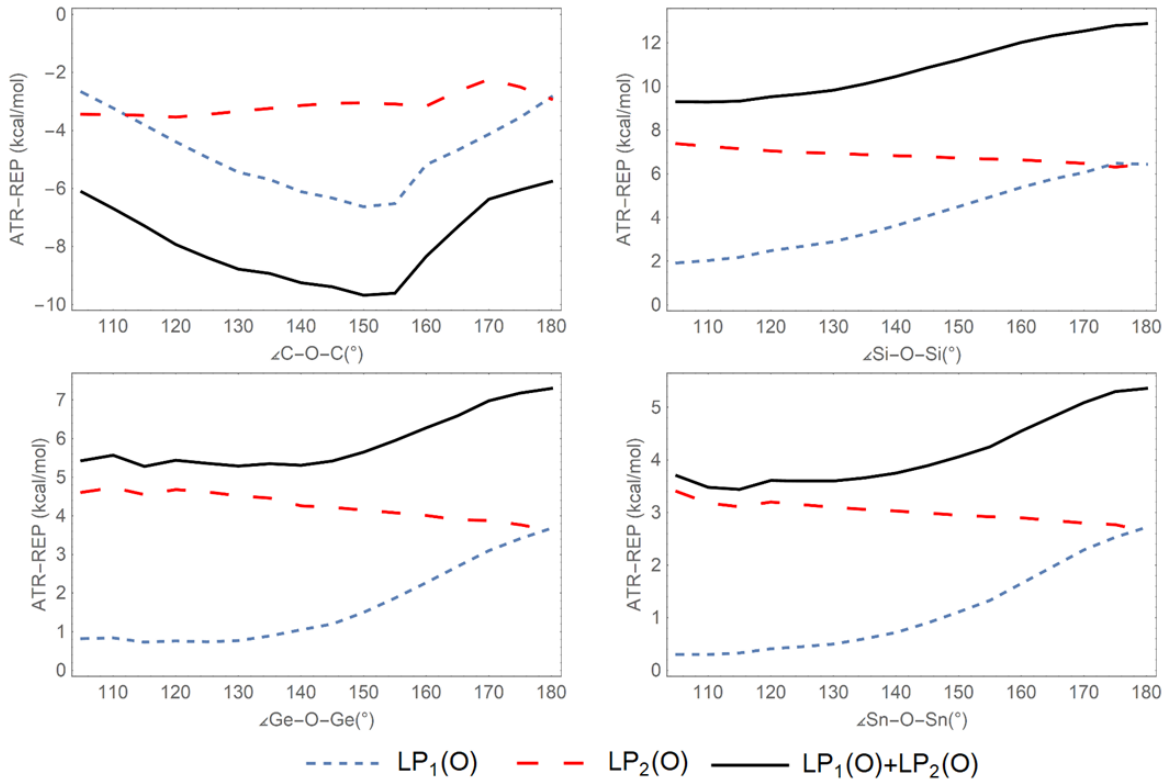

Figure 1.7. Calculated energy offsets between attractions and repulsions originating in $LP_1(O)$ and $LP_2(O)$, for model $(H_3E)_2O$ derivatives (E = C, Si, Ge, Sn).

Organic *vs.* Inorganic Hydrogenated and Methylated Alcohols

The next class of derivatives investigated is that of $(R_3E)OH$ species (E = C, Si, Ge, Sn; R = H, Me). The equilibrium geometries of such E-O-H systems largely reproduce features previously determined for E-O-E units: *e.g.* inorganic counterparts exhibit E-O bond distances that are considerably shorter than expected values, while E-O-H angles (E = Si, Ge, Sn) are always larger than C-O-H. In short, the different structural behaviour between organic and inorganic $(R_3E)OH$ analogues is explained in the same way as for $(R_3E)_2O$ derivatives, based on offsets between attractive and repulsive interactions occurring at the E-O bond level (see ***Figure 1.8***). The influence of attractive LP(O)→σ*(E-R) + LP(O)→d(E) interactions (E = Si, Ge and Sn) on the structures of inorganic E-O-H model systems is further demonstrated by NBO DEL optimizations.

The results obtained on $(R_3E)OH$ models reinforce conclusions determined on ethers, contributing to the development of a general model for the E-O chemical bond.

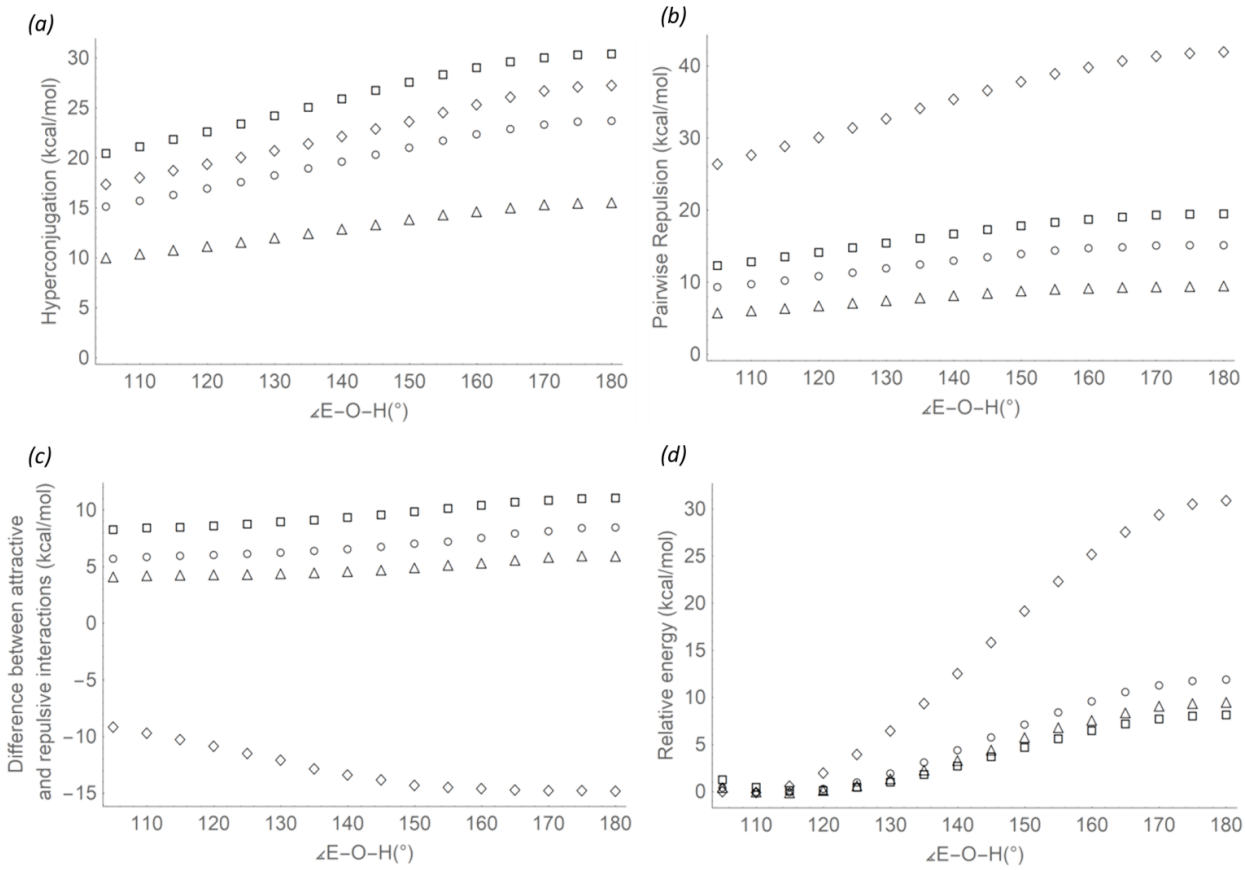

Figure 1.8. Calculated E-O-H angle dependence of: (a) total attraction energy per E-O bond; (b) total Pauli repulsion energy per E-O bond; (c) attraction-repulsion offsets per E-O bond; (d) molecular energy, for model $(Me_3E)OH$ derivatives (E = C – ◇, Si – □, Ge – ○, and Sn – △). Similar trends were obtained for $(H_3E)OH$ counterparts (these were illustrated in the main thesis manuscript).

Organic *vs.* Inorganic Halogenated Ethers

DFT explorations of halogenated ethers aim at evaluating whether the substitution of hydrogen atoms with more electronegative groups, such as the fluorine and chlorine ligands, brings some fundamental changes into the bonding mechanism of E-O-E linkages. Equilibrium E-O-E angles and E-O bond distances of model $(H_3E)_2O$, $(XH_2E)_2O$, and $(X_2HE)_2O$ ethers (X = F or Cl) (***Table 1.8***) suggest that he substitution of hydrogen ligands with halogen groups trigger the length contraction of the E-O bonds, while E-O-E angle widening is observed especially for the organic ethers.

Table 1.8. Equilibrium E-O-E angles and E-O bond lengths of model hydrogenated/halogenated compounds

E	$(H_3E)_2O$		$(XH_2E)_2O$; X = F / Cl		$(X_2HE)_2O$; X = F /Cl		Σ*cov*(E+O) (Å) [*ref. 35*]
	E-O-E (°)	E-O (Å)	E-O-E (°)	E-O (Å)	E-O-E (°)	E-O (Å)	
C	112.1	1.399	114.8 / 116.1	1.381 / 1.380	121.0 / 126.3	1.376 / 1.378	*1.42*
Si	148.7	1.636	154.4 / 148.1	1.621 / 1.627	159.1 / 151.8	1.610 / 1.620	*1.77*
Ge	128.1	1.773	130.6 / 130.6	1.758 / 1.763	134.1 / 135.2	1.743 / 1.754	*1.86*
Sn	133.5	1.954	131.1 / 132.1	1.941 / 1.945	135.9 / 135.7	1.926 / 1.935	*2.05*

The structural differences between halogenated and hydrogenated ethers are further explained in terms of attraction-repulsion offsets generated separately by $LP_1(O)$ and $LP_2(O)$ (***Figure 1.9***). Thus, the weak dependence of the $LP_1(O)$ offset value on the number of halogen substituents in the series of inorganic $(H_3E)_2O$, $(XH_2E)_2O$, and $(X_2HE)_2O$ derivatives motivates the almost equal values of the E-O-E angles (*i.e.* fluorinated siloxanes are an exception from this rule). The same $LP_1(O)$ offset explains the variation of the C-O-C angle in organic ethers. Regarding $LP_2(O)$, attraction-repulsion energy counterbalances originating in this lone pair successfully

explain the contraction of E-O bond length in halogenated species, both for organic and inorganic counterparts.

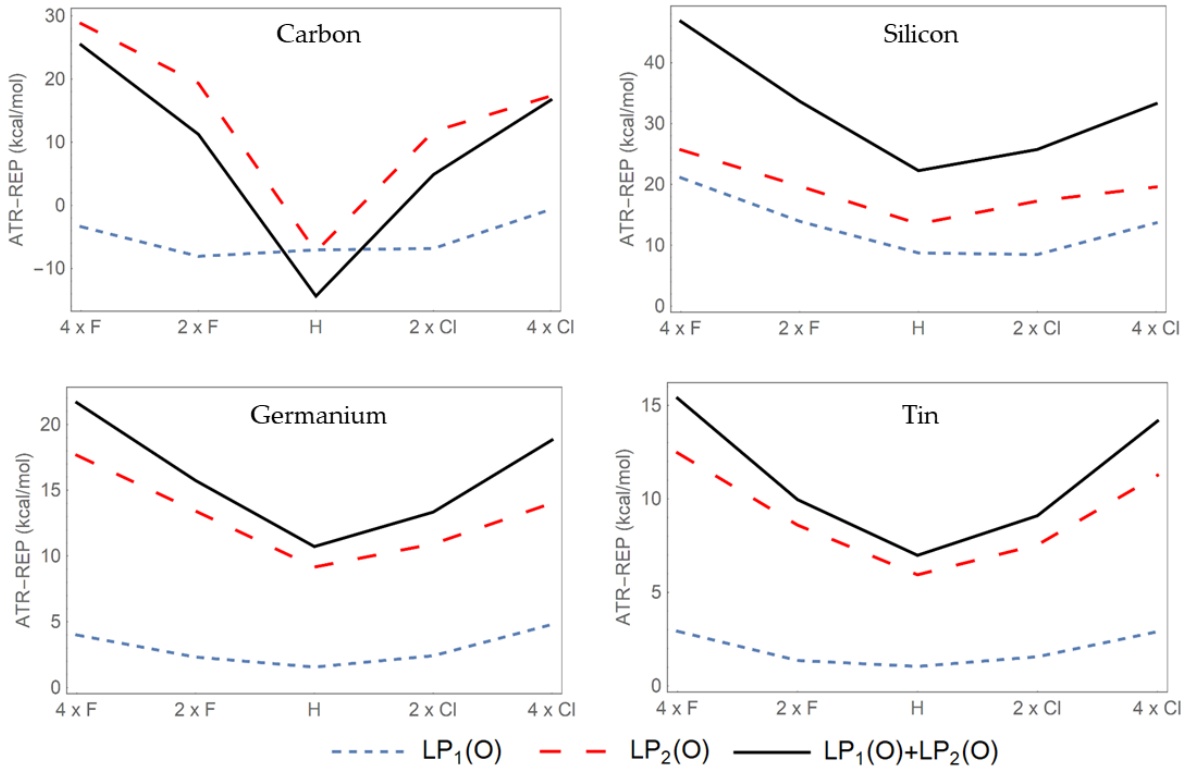

Figure 1.9. Attraction-repulsion offsets per E-O-E unit for $LP_1(O)$, $LP_2(O)$, along with the total offset energy per E-O-E unit, *i.e.* $LP_1(O)+LP_2(O)$, are plotted as a function of the number of halogen atom substituents within the following series of model compounds: $(H_3E)_2O$, $(XH_2E)_2O$, and $(X_2HE)_2O$.

These results are in line with the conclusions on the $(R_3E)_2O$ models and reinforce the belief that s/p and the p lone pairs dictate the structural features of the E-O-E moiety in different manners.

Organic *vs.* Inorganic Acyclic E-O-E Oligomers

The next type of derivatives investigated is that of oligomers containing two/three E-O-E units, such as the H_3E-O-EH_2-O-EH_3 and H_3E-O-EH_2-O-EH_2-O-EH_3 models (***Figure 1.10***).

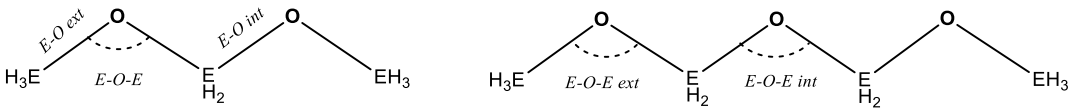

Figure 1.10. Model acyclic oligomers incorporating two (*left side*) and respectively three (*right side*) E-O-E units.

The structural features determined for such species are further explained on the basis of the attraction-repulsion bond model. For instance, the internal E-O bonds of H_3E-O-EH_2-O-EH_3 oligomers exhibit shorter lengths than the external ones (see ***Table 1.9***). However, such differences are successfully explained in terms of attraction-repulsion offset generated by LP_2(O). Attraction-repulsion offset originating in LP_1(O) also motivate the widening differences between the external and the internal E-O-E angles of H_3E-O-EH_2-O-EH_2-O-EH_3 species.

Table 1.9. Equilibrium E-O bond lengths of H_3E-O-EH_2-O-EH_3 acyclic oligomers and the related attraction-repulsion offset generated by LP_2(O).

H_3E-O-EH_2-O-EH_3				
E	**E-O int (Å)**	**E-O ext (Å)**	**LP_2(O) offset / int E-O bond (kcal mol^1)**	**LP_2(O) offset / ext E-O bond (kcal mol^{-1})**
C	1.392	1.409	113.6	113.5
Si	1.626	1.637	148.3	147.9
Ge	1.766	1.778	129.9	127.8
Sn	1.949	1.959	135.5	127.3

Organic *vs.* Inorganic Oxonium Cations

Model derivatives of the $[(R_3E)_3O]^+$ and $[(R_3E)_2OH]^+$ type are further investigated, paying particular attention to understanding the structural contrast between organic and inorganic counterparts, *i.e.* the E_3O skeletons (E = Si, Ge, Sn) of inorganic derivatives are planar while the C_3O fragments are pyramidal. Nevertheless, these differences are easy to explain in terms of attractions and repulsions (***Figure 1.11***), by employing the same bonding mechanism that has proved to be a successful strategy for neutral E-O-E systems. The maximization of the attraction-repulsion offsets towards larger E-O-E angles (E = Si, Ge, Sn) motivates the planar geometries of inorganic oxonium ions, while opposite trends for the organic cations are consistent with their pyramidal structures.

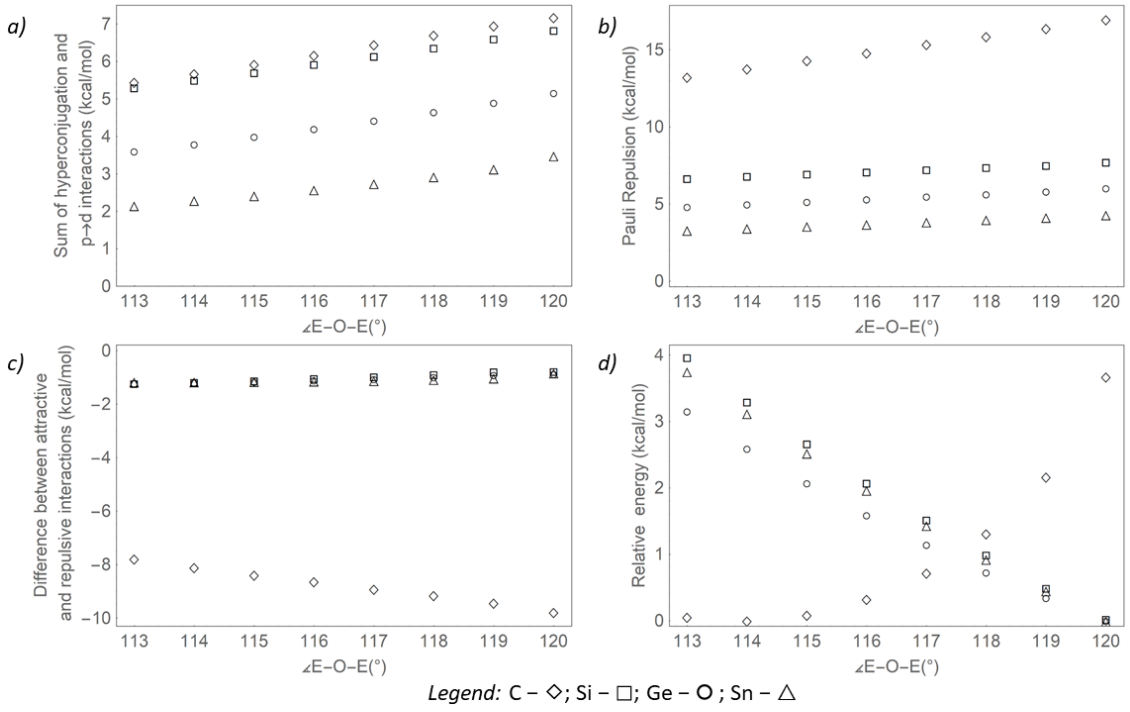

Figure 1.11. Computed E-O-E angle dependence of: (a) total attraction energy; (b) total Pauli repulsion energy; (c) attraction-repulsion offset energy; (d) molecular energy, per E-O bond, for model $[(H_3E)_3O]^+$ oxonium cations (E = C – ◇, Si – □, Ge – ○, and Sn – △).

Organic *vs.* Inorganic Amines

Finally, the last sub-section of this first chapter concerns the bonding mechanism of amines and their inorganic counterparts. Model derivatives investigated are of the $(R_3E)_3N$, $(R_3E)_2NH$ and $(R_3E)NH_2$ type. As in the case of oxonium cations, which are *inter alia* isoelectronic with amines, the study focuses on explaining the different shapes between the organic C_3N and inorganic E_3N (E = Si, Ge, Sn) skeletons. Again, this is only possible when the interplay between attractive and repulsive secondary electronic effects is considered (***Figure 1.12***). Therefore, the bonding model proposed in this study is quite general, including both E-O and E-N bonds, with prospects for extension to other heavier p-block elements.

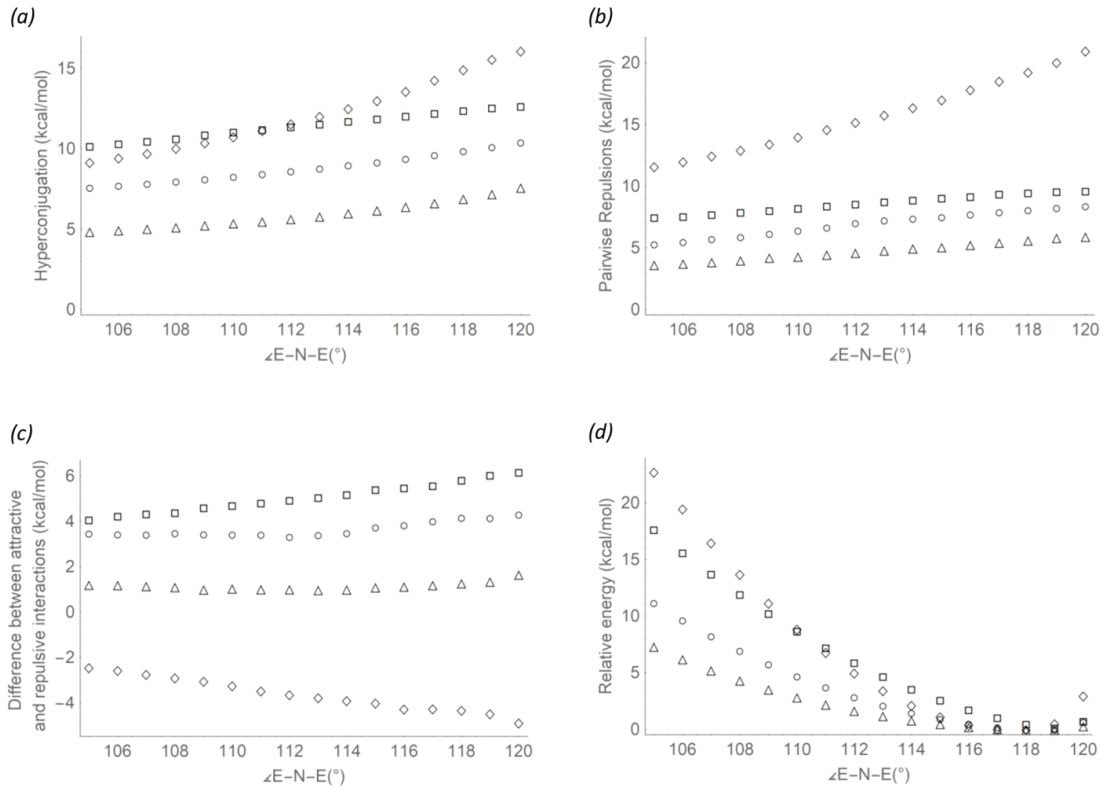

Figure 1.12. Computed E-N-E angle dependence of: (a) total attraction energy; (b) total Pauli repulsion energy; (c) attraction-repulsion offset energy; (d) molecular energy, per E-N bond, for model hydrogenated $(H_3E)_3N$ amines (E = C – ◇, Si – □, Ge – ○, and Sn – △).

1.3 Brief Summary

A new bonding mechanism based on the interplay between attractive (hyperconjugations and p→d donations) and repulsive (Pauli repulsions) electronic effects is developed. The current approach fills some gaps of existing bond models and successfully explains the structural features (including the organic versus inorganic contrast) of a wide range of model compounds that incorporate the E-O-E, E-O-H, E_3N, E_2NH and ENH_2 fragments (E = C, Si, Ge, Sn).

The results presented in this chapter were disseminated through the publication of three scientific articles, as follows:

1. Bridging a Knowledge Gap from Siloxanes to Germoxanes and Stannoxanes. A Theoretical Natural Bond Orbital Study
   I.-T. Moraru, P. M. Petrar and G Nemes*, *J. Phys. Chem. A*, 2017, **121**, 2515−2522.

2. Theoretical Insights into the Structural Differences between Organic and Inorganic Amines/Ethers
   I.-T. Moraru*, F. Teleanu and G Nemes*, *J. Phys. Chem. A*, 2020, **124**, 8246-8253.

3. Offsets between hyperconjugations, p→d donations and Pauli repulsions impact the bonding of E–O–E systems. Case study on elements of Group 14
   I.-T. Moraru*, F. Teleanu, L. Silaghi-Dumitrescu and G Nemes*, *Phys. Chem. Chem. Phys.*, 2022, **24**, 13217-13228.

1.4 Selected References

(1) R. West, L. S. Wilson and D. L. Powell, J*. Organomet. Chem*., 1979, **178**, 5.

(2) B. D. Shepherd, *J. Am. Chem. Soc*., 1991, **113**, 5581.

(3) J. Passmore and J. M. Rautiainen, *Eur. J. Inorg. Chem.*, 2012, **2012**, 6002

(4) F. Weinhold and R. West, *Organometallics*, 2011, **30**, 5815

(5) F. Weinhold and R. West, *J. Am. Chem. Soc*., 2013, **135**, 5762.

(6) G. V. Gibbs, A. F. Wallace, D. F. cox, R. T. Downs, N. L. Ross and K. M. Rosso, *Amer. Mineral*., 2009, **94**, 1085.

(7) S. Grigoras and T. H. Lane, *J. Comput. Chem*., 1988, **9**, 25.

(8) S. Grigoras and T. H. Lane, *J. Comput. Chem*., 1987, **8**, 84.

(9) S. Shambayati, S. L. Schreiber, J. F. Blake, S. G. Wierschke and W. L. Jorgenson, *J. Am. Chem. Soc*., 1990, **112**, 697.

(10) M. Cypryk and Y. Apeloig, *Organometallics*, 1997, **16**, 5938.

(11) M. Cypryk, *Macromol. Theory Simul*., 2001, **10**,158.

(12) I. Bakk, Á. Bóna, L. Nyulászi and D. Szieberth, *J. Mol. Struct.:THEOCHEM*, 2006, **770**, 111.

(13) G. V. Gibbs, M. B. Boisen, F. C. Hill, O. Tamada and R. T. Downs, *Phys. Chem. Miner*., 1998, **25**, 574.

(14) C. Martín-Fernández, I. Alkorta, M. M. Montero-Campillo and J. Elguero, *ChemPhysChem*, 2022, **23**, e202200088

(15) R. J. Gillespie and S. A. Johnson, *Inorg. Chem*., 1997, **36**, 3031.

(16) S. Grabowsky, M. F. Hesse, C. Paulmann, P. Luger and J. Beckmann, *Inorg. Chem*., 2009, **48**, 4384.

(17) M. Fugel, M. F. Hesse, R. Pal, J. Beckmann, D. Jayatilaka, M. J. Turner, A. Karton, P. Bultinck, G. S. Chandler and S. Grabowsky, *Chem. Eur. J.*, 2018, **24**, 15275.

(18) P. Livant, M. L. McKee and S. D. Worley, *Inorg. Chem*., 1983, **22**, 895.

(19) Y. Mo, Y. Zhang and J. Gao, *J. Am. Chem. Soc*., 1999, **121**, 5737.

(20) Y. V. Vishnevskiy, M. A. Abaev, A. A. Ivanov, L. V. Vilkov and M. Dakkouri, *J. Mol. Struct*., 2008, **889**, 316.

(21) D. B. Beach and W. L. Jolly, *Inorg. Chem*., 1984, **23**, 4774.

(22) E. W. Olson and J. M. Standard, *J. Mol. Struct.: THEOCHEM*, 2005, **719**, 17.

(23) F. Dankert, R. Richter, F. Weigend, X. Xie, M. Balmer and C. von Hänisch, *Angew. Chem. Int. Ed*., 2021, **60**, 10393.

(24) F. Dankert and C. von Hänisch, *Inorg. Chem.*, 2019, **58**, 3518.

(25) M. R. Buchner, M. Müller, F. Dankert, K. Reuter and C. von Hänisch, *Dalton Trans*., 2018, **47**, 16393.

(26) J. Pahl, H. Elsen, A. Friedrich and S. Harder, *Chem. Commun*., 2018, **54**, 7846.

(27) R. West, L. S. Whatley and K. J. Lake, *J. Am. Chem. Soc*., 1961, **83**, 761.

(28) C. G. Pitt, M. M. Bursey and D. A. Chatfield, *J. Chem. Soc., Perkin Trans*., 1976, **2**, 434.

(29) C. G. Pitt, J. Organomet. Chem., 1973, **61**, 49.

(30) C. J. Rhodes, *J. Chem. Soc., Perkin Trans.*, 1992, **2**, 235.

(31) I. V. Alabugin, G. dos Passos Gomes and M. A. Abdo, *Wires*, 2019, **9**, e1389.

(32) I. V. Alabugin, L. Kuhn, N. V. Krivoshchapov, P. Mehaffy and M. G. Medvedev*, Chem. Soc. Rev*., 2021, **50**, 10212.

(33) I. V Alabugin and T. A. Zeidan, *J. Am. Chem. Soc*., 2002, **124**, 3175.

(34) P. v. R. Schleyer and A. J. Kos, *Tetrahedron*, 1983, **39**, 1141.

(35) B. Cordero, V. Gomez, A. E. Platero-Prats, M. Reves, J. Echeverria, E. Cremades, F. Barragan and S. Alvarez, *Dalton Trans*., 2008, **21**, 2832.

(36) K. Tamagawa, M. Takemura, S. Konaka and M. Kimura, *J. Mol. Struct*., 1984, **125**, 131.

(37) S. Liedle, H.-G. Mack, H. Oberhammer, M. R. Imam and N. L. Allinger, *J. Mol. Struct.*, 1989, **198**, 1.

(38) T. V. Timofeeva, I. L. Dubchak, V. G. Dashevsky and Yu. T. Struchkov, *Polyhedron*, 1984, **3**, 1108.

(39) A. Almenningen, O. Bastiansen, V. Ewing, K. Hedberg and M. Traetteberg, *Acta Chem. Scand.*, 1963, **17**, 2455.

(40) C. Glidewell, D.W. H. Rankin, A. G. Robiette, G. M. Sheldrick, B. Beagley and S. Cradock, *J. Chem. Soc. A*, 1970, 315.

(41) L. V. Vilkov and N. A. Tarasenko*, J. Struct. Chem*., 1969, **10**, 979.

Chapter 2

Insights into carbide formation during CO hydrogenation catalysed by ultra-small ruthenium nanoparticles: a DFT investigation

2.1 Introduction and Literature Data

This second chapter consists in a comprehensive computational chemistry study addressing some fundamental questions related to the formation of carbides on the surface of ultra-small ruthenium nanoparticles (RuNPs), in the context of the CO hydrogenation process.

Computational chemistry has become a relevant tool in the field of heterogeneous catalysis during the last twenty years,[1-7] in part thanks to the continued progress of computing resources, but also due to the development of dedicated software packages. The common goal of the theoretical community interested in the rational design of such catalysts is to simulate as close as possible experimental structures.[3] Special attention is paid to metal nanoparticles (MNPs),[8,9] given their increased catalytic activity over bulk metal materials.

Among other technological processes, MNPs are active catalysts for the Fischer-Tropsch synthesis (FTS).[10,11] From a mechanistic viewpoint,[12-14] FTS reveals a considerably complex reaction scheme given that involves a very large number of intermediates but also several competing pathways. The key step in FTS is most probably the CO bond-breaking step, given the increased stability of this triple carbon-oxygen chemical bond, generally accepted mechanisms being illustrated in ***Figure 2.1***

According to literature data, the most active catalysts in the FT process are MNPs based on iron,[15-18] cobalt[19-22] and ruthenium.[23-25] In case of Fe-based FTS, iron-carbides are undoubtedly more efficient than pure metallic analogous.[16-18] For cobalt, carbides have rather poisoning effects, while for ruthenium only pure metallic catalysts are known.[26-30]

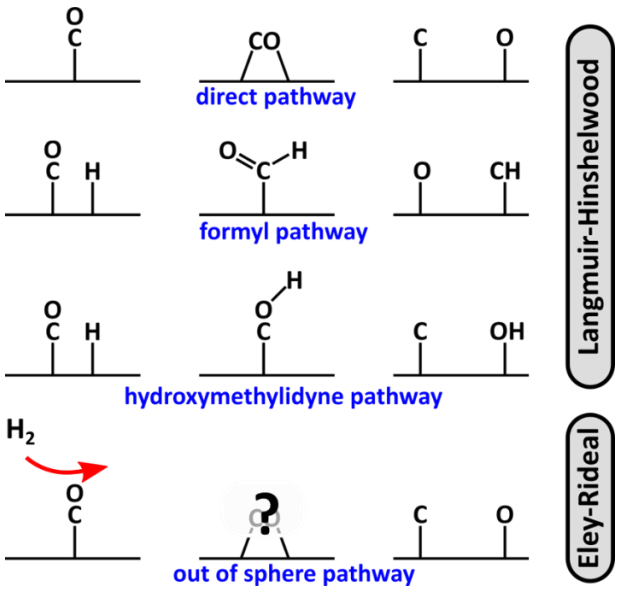

Figure 2.1. Schematic representation of the generally accepted mechanisms related to the CO dissociation step of the FT process

Although the formation of carbides on ruthenium surfaces[26,27,31-34] has been proposed theoretically, it has never been firmly confirmed experimentally. Still, most of the theoretical models employed in these studies were not realistic, at least not in terms of surface composition. According to Cusinato *et al.,*[35] under normal FT conditions the surfaces of RuNPs are saturated with CO ligands (*ca.* 1.5 CO ligands/surface Ru atom), while H_2 co-adsorption is very low, most probably in traces. The same study emphasized the possible formation of stable carbides at the surface of RuNPs, but without discussing their kinetic accessibility.

The presence of carbides on RuNPs remains an open topic in the context of CO hydrogenation. It is insightful to understand whether such surface species (transient or not) have any influence on the catalytic properties of ruthenium nanoclusters.

2.2 Original contributions

DFT calculations are carried out on Ru_{55} model nanoclusters (***Figure 2.2***), which are similar in terms of size, shape and surface composition to the synthesized RuNPs (***Figure 2.3***). Such models are employed in the following mechanistic explorations.

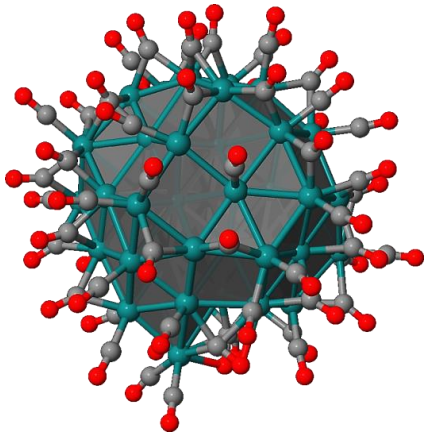

Figure 2.1. Theoretical Ru_{55} nanocluster model intended to replicate the experimental conditions

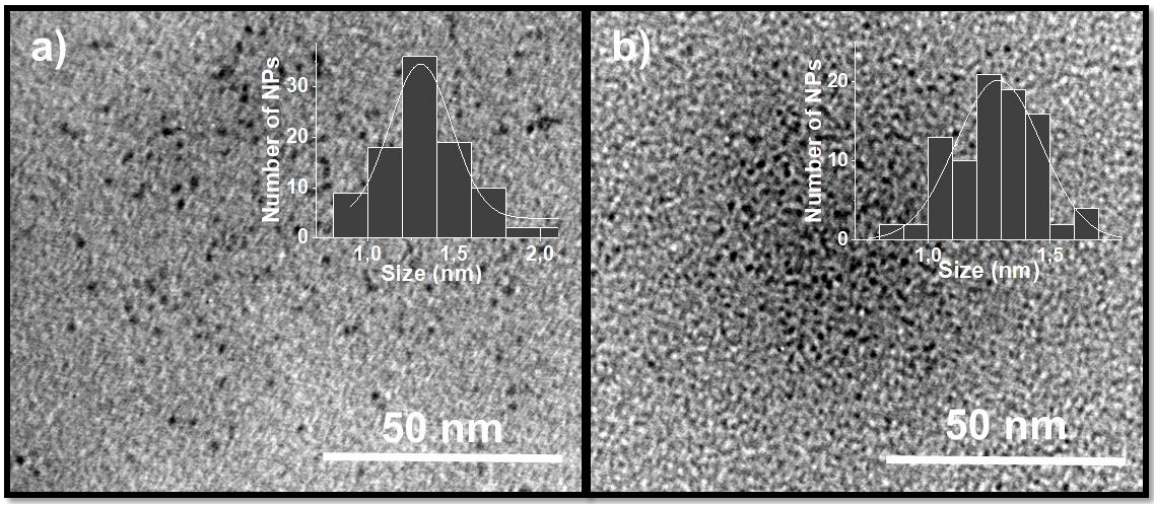

Figure 2.2. TEM characterization of the synthesized Ru NPs (stabilized by PVP) (**a**) before catalytic conditions and (**b**) after catalytic conditions.

DFT investigations of carbide formation mechanisms

The first DFT pathway addresses the possible formation of surface ruthenium carbides in a standard four-fold site of the model nanocluster, via a hydrogen-assisted mechanism that involves adsorbed hydroxymethylidyne (COH*) species (***Figure 2.3***). Co-adsorption of one H_2 molecule on the CO-saturated surface of the $Ru_{55}(CO)^*_{66}$ NP is slightly endothermic, but the subsequent transformations are exothermic and occur at reasonable kinetic cost. Finally, a very stable μ_5 carbide (C*) is formed in the presence of water.

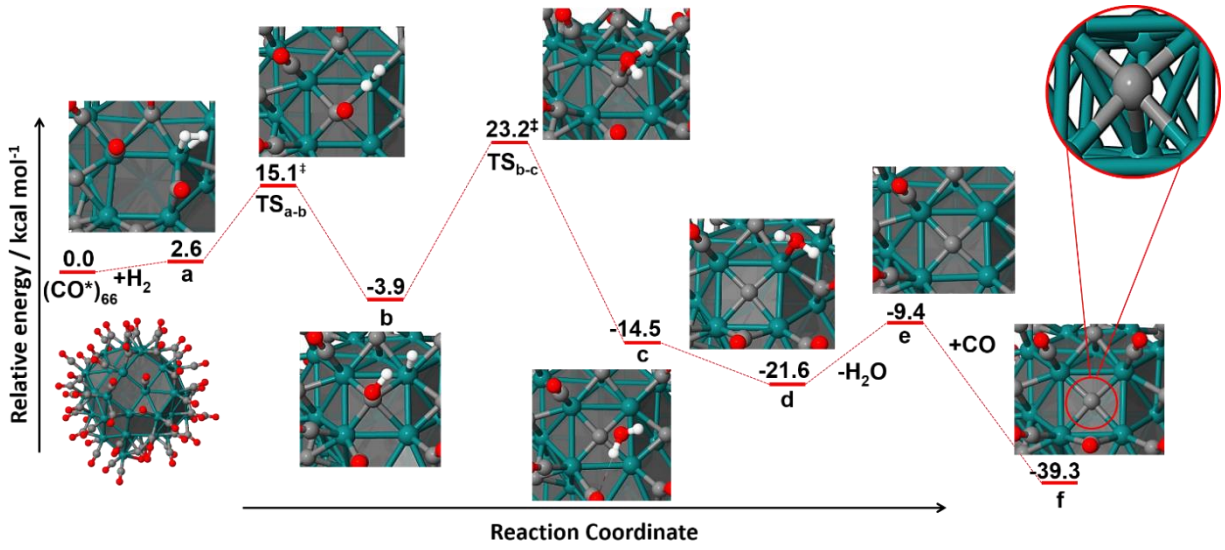

Figure 2.3. CO dissociation pathway involving carbide formation in a standard four-fold site on the 101 face of the Ru_{55} nanocluster

Mechanistic investigations additionally indicate the formation of μ_5-C* species in the B_5 site, via COH* intermediates. In fact, for this defective site DFT calculations suggest two concurrent pathways (***Figures 2.5*** and ***2.6***). In both cases, stable surface carbides are formed, while barrier heights are relatively low in the context of the Fischer-Tropsch process.

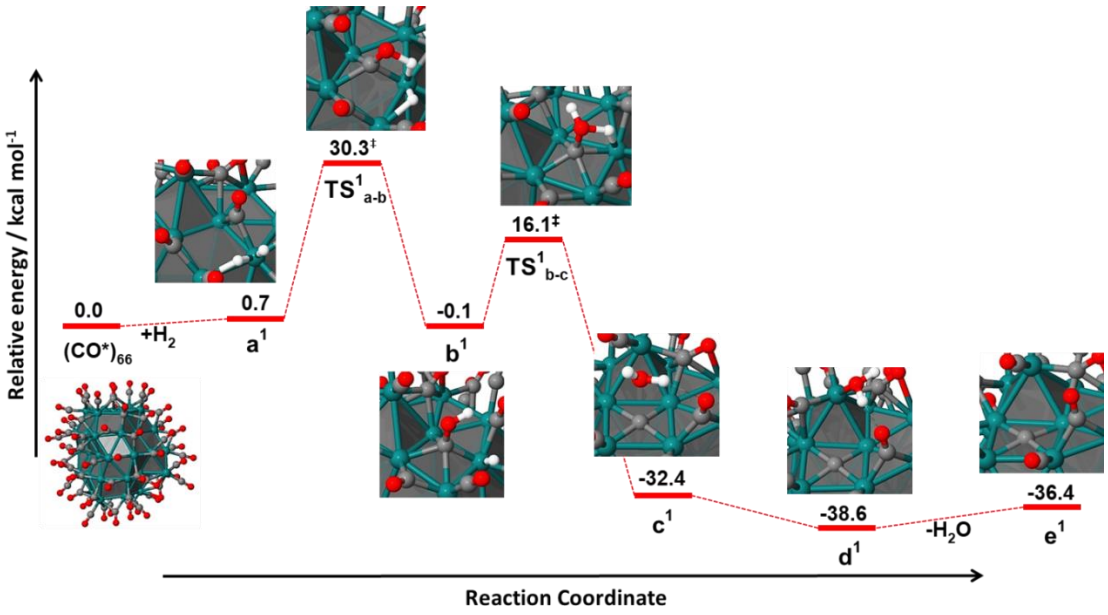

Figure 2.4. The first mechanism illustrating the formation of stable μ_5-carbide at the bottom of the B_5 site via COH intermediates

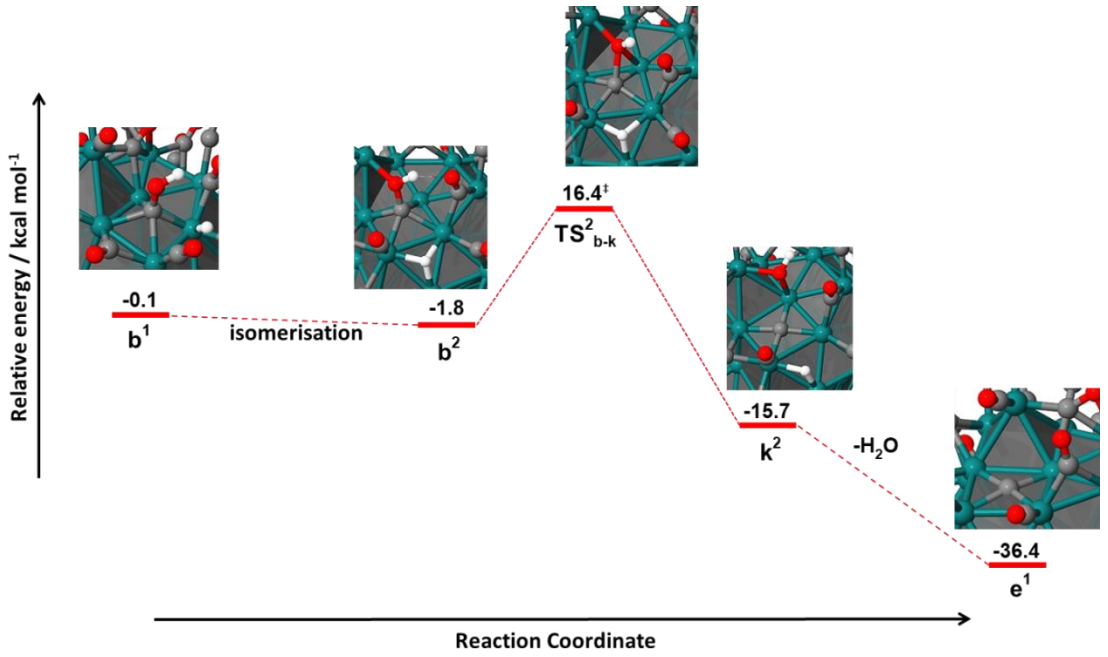

Figure 2.5. The second hydroxymethylidyne mechanism highlighting the formation of stable μ_5-carbide at the bottom of the B_5 defective site.

The possible presence of μ_3 surface carbides is also evaluated (***Figure 2.7***). According to computed energies, these species are considerably less stable than the μ_5 carbides and involve endothermic transformations. Further stabilization of the μ_3-C* species is obtained if the released gaseous water molecule coordinates nearby the carbide, as in **d^3**, either by adsorption in its vicinity of a CO ligand, as in **f^3**.

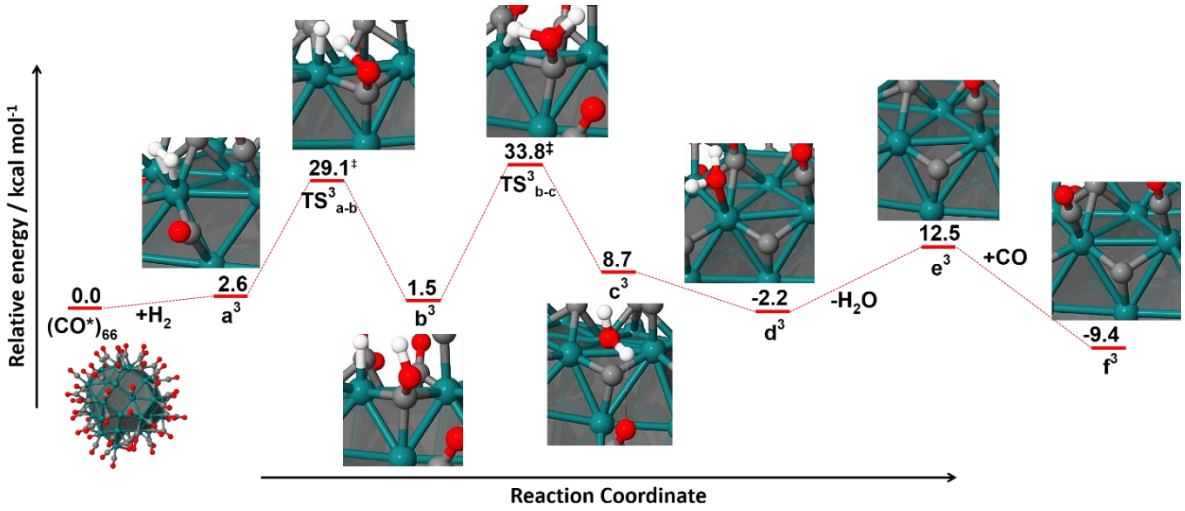

Figure 2.6. DFT mechanism highlighting μ_3-carbide formation on standard three-fold sites on the metal surface of the Ru_{55} nanocluster.

Another mechanism illustrates the formation of a stable μ_6-carbide (***Figure 2.8***). This is a very interesting side result given that the formation of such μ_6-C* species has not been suggested so far on RuNPs, although such carbides are quite common for molecular ruthenium clusters. This pathway reveals the lowest barriers among all investigated routes, but in occurs under the tip ruthenium atom, a site scarcely present on metal NPs. Other DFT explorations suggest the formation of stable μ_5 carbides in the proximity of the B_5 site (***Figure 2.9***). This last pathway brings a surprising, but very interesting side result, highlighting the formation of a highly stable surface species: a pseudo-octahedral ruthenium molecular complex of the $Ru(CO)_3(OC)(Ru_{54})$ type. Such a surface complex has never been reported before on RuNPs.

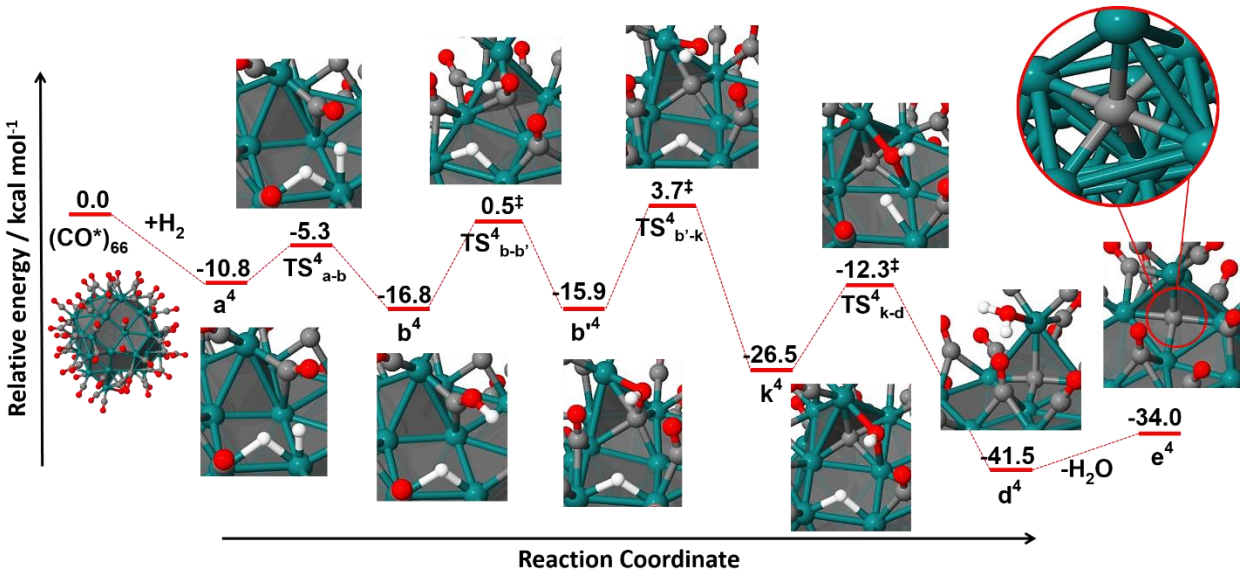

Figure 2.8. A DFT calculated hydroxymethylidyne route leading to the formation of a μ_6 carbide under the tip ruthenium atom of the B_5 site.

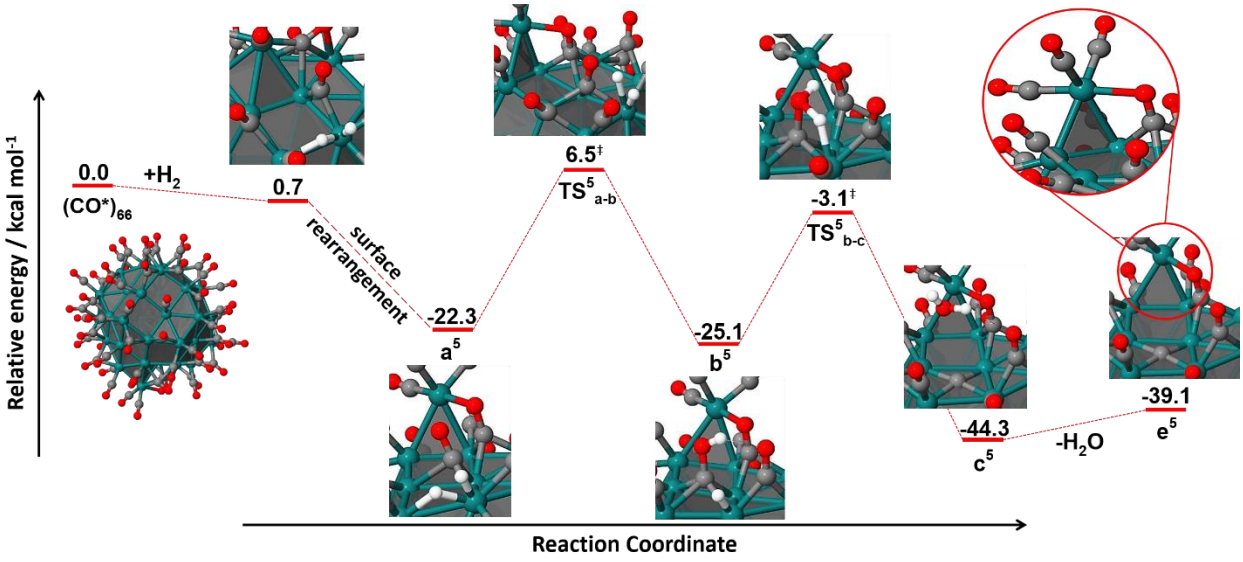

Figure 2.9. Hydroxymethylidyne pathway depicting carbide formation in a four-fold site located close to a surface molecular complex.

The last mechanism considered is that of a direct CO dissociation route (***Figure 2.10***). Formation of the μ_5 carbide involve a highly endothermic transformation, in stark contrast to the case of hydroxymethylidyne mechanisms illustrated above. These results are in agreement previous findings,[36,37] reinforcing that direct dissociation pathways are unlikely to occur on crowded CO surfaces (*i.e.* corresponding to actual experimental conditions).

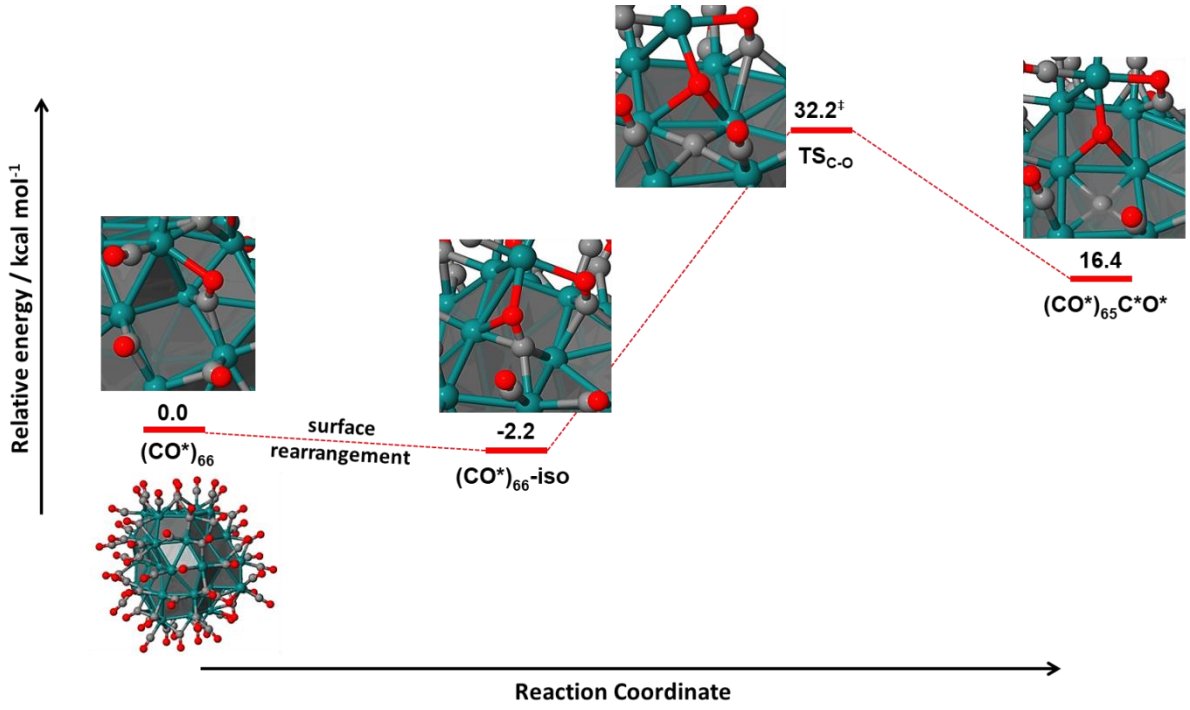

Figure 2.7. Direct dissociation route computed for a CO molecule that is adsorbed at the bottom of the defective B_5 site.

As a corollary, the DFT mechanistic study highlighted that stable ruthenium μ_5-carbides are formed systematically on standard four-fold sites of the RuNPs via hydroxymethylidyne pathways, while μ_3-carbides can be as well obtained through COH intermediates, although in harsher conditions.

NMR studies

To confirm the novel theoretical findings related to the presence of stable carbides on ruthenium nanoclusters, ^{13}C-NMR experimental studies were carried out in collaboration on ultra-small RuNPs exhibiting diameters of *ca.* 1 nm (*i.e.* dimensions are similar to the Ru_{55} theoretical model). Measured spectra (on RuNPs after catalytic conditions) are illustrated in ***Figure 2.11*****8**, the broad signal at *ca.* 360 ppm being attributed to ruthenium surface carbides.

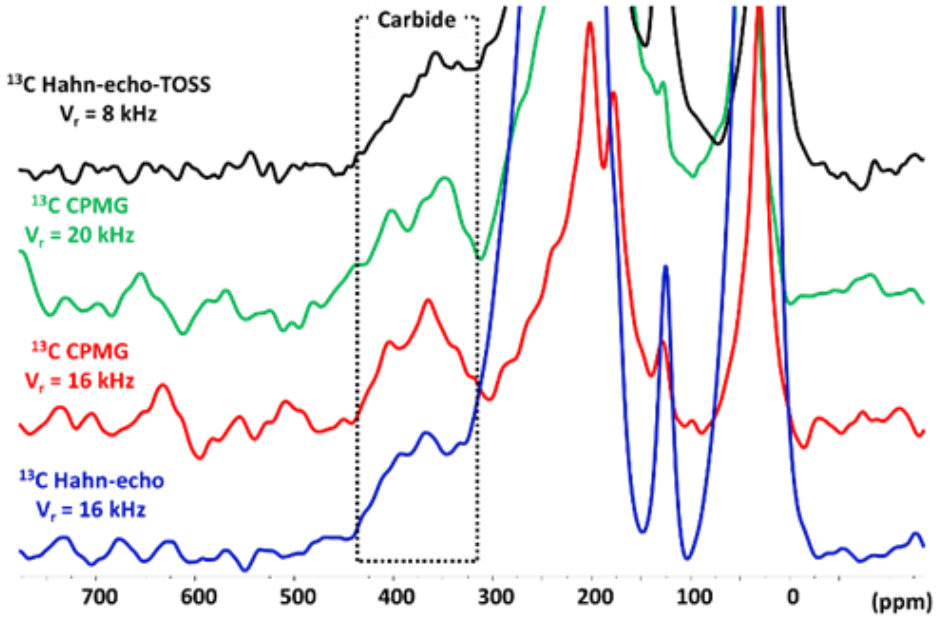

Figure 2.19. Solid-state ^{13}C-NMR spectra focusing on the ca. 360 ppm resonance signal corresponding to a ruthenium surface carbide.

DFT-NMR explorations are performed on ruthenium clusters (used as scale models to mimic the adsorption sites of RuNPs) to ensure that the experimental NMR data has been assigned correctly. Ruthenium carbonyl clusters of the $[Ru_5]$ type (***Figure 2.12***) are employed to compute the ^{13}C chemical shifts of the μ_5 carbides. It appears to be 382 ppm for the $[Ru_5](CO)_4$ model (***Figure 2.12*****a**), value that is close to the experimental signal observed at *ca.* 360 ppm. In fact, the $[Ru_5](CO)_4$ cluster represents the best scale model, among the $[Ru_5](CO)_x$ series (x = 0 – 4), that reproduces the environment around a carbide adsorbed on 4-fold site on the Ru_{55} NP.

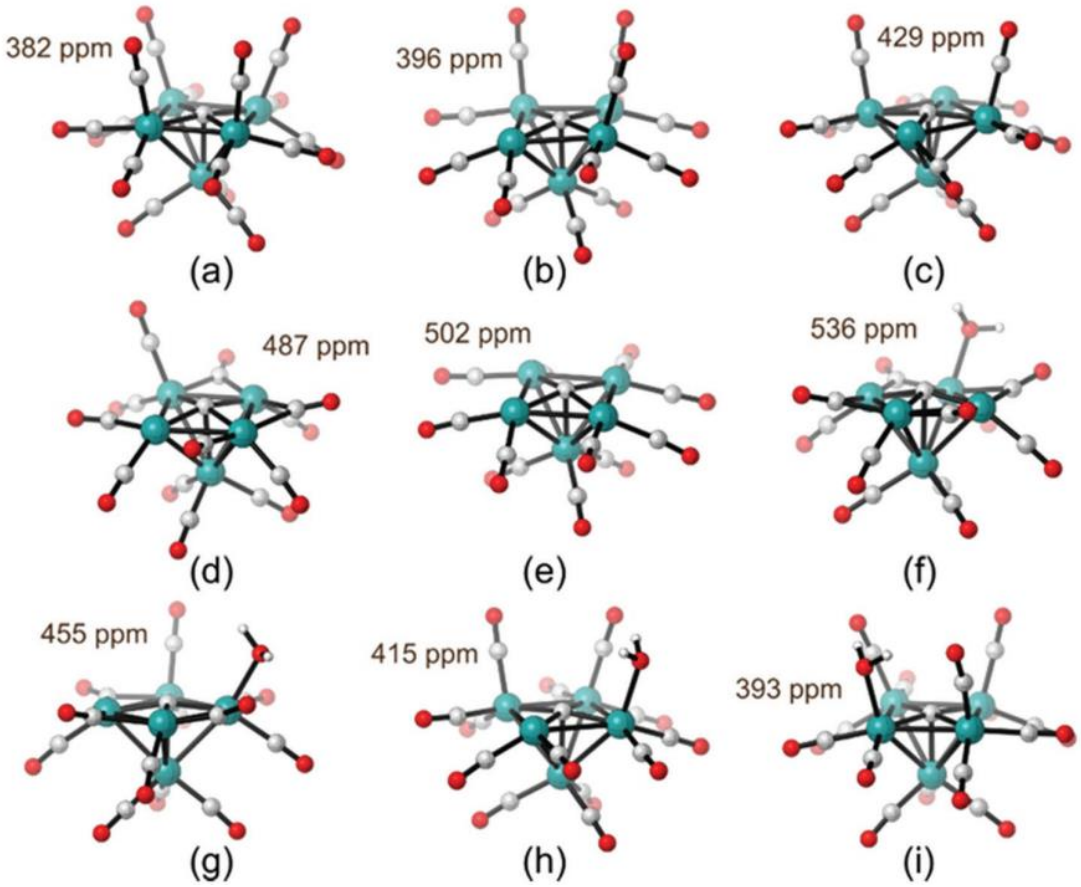

Figure 2.12. Calculated ^{13}C chemical shifts for the following model clusters: (**a**) $[Ru_5](CO)_4$; (**b**) $[Ru_5](CO)_3$; (**c**) $[Ru_5](CO)_2$; (**d**) $[Ru_5](CO)$; (**e**) $[Ru_5]$; (**f**) $[Ru_5](OH_2)$; (**g**) $[Ru_5](CO)(OH_2)$; (**h**) $[Ru5](CO)_2(OH_2)$; and (**i**) $[Ru5](CO)_3(OH_2)$.

In addition, DFT-NMR calculations indicate that the 360 ppm resonance corresponds unambiguously to a carbide and not to other possible formed intermediates, such as ketenylidene (CCO*), methine (CH*) or methylene (CH_2*) species (see ***Figure 2.13***).

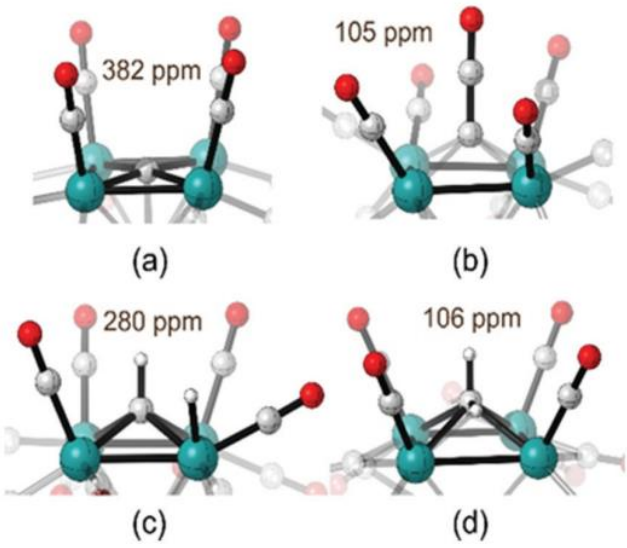

Figure 2.13. Calculated ^{13}C chemical shifts for the following model clusters: (**a**) $[Ru_5](CO)_4$; (**b**) $[Ru_5](CO)_4(CCO)$; (**c**) $[Ru_5](CO)_4(CH)(H)$; (**d**) $[Ru_5](CO)_4(CH_2)$.

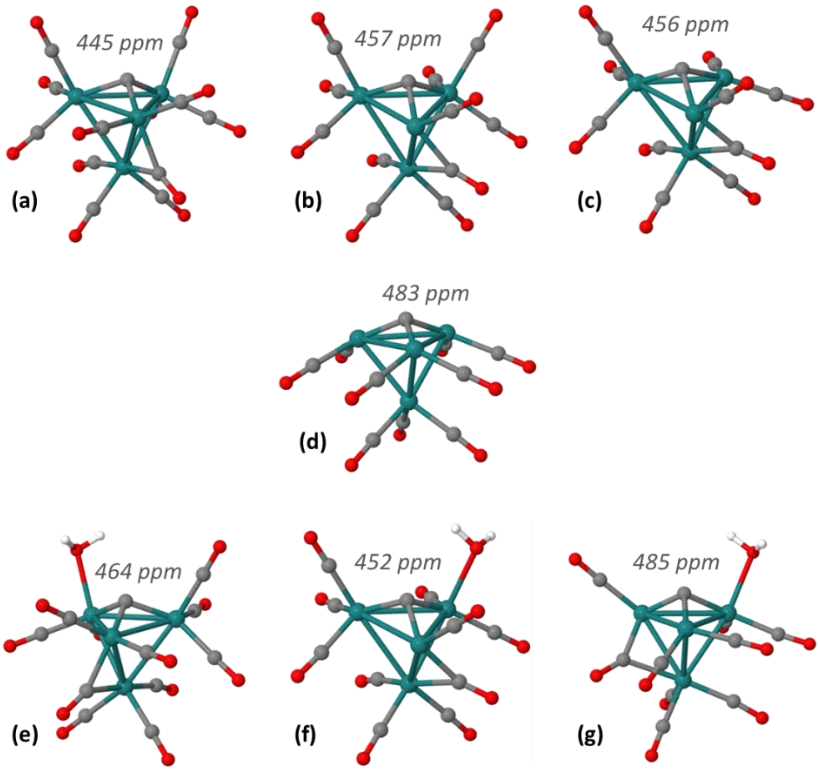

Figure 2.14. Calculated ^{13}C chemical shifts for the following model clusters: (**a**) $[Ru_4](CO)_3$; (**b**) $[Ru_4](CO)_2$; (**c**) $[Ru_4](CO)$; (**d**) $[Ru_4]$; (**e**) $[Ru_4](OH_2)$; (**f**) $[Ru_4](CO)(OH_2)$; (**e**) $[Ru_4](CO)_2(OH_2)$.

The chemical shifts of μ_3 carbides are also calculated on several [Ru_4] and [Ru_6] model clusters, which are intend to replicate the three-fold sites of the Ru_{55} NP (see ***Figures 2.14*** and ***2.15*****a,b**). However, the chemical shifts for such μ_3-carbide species are never lower than 433 ppm, value that is notably higher than the experimental 360 ppm one. It is also clear that this resonance signal does not correspond to a ketenylidene, methine or methylene surface species, potentially formed from the μ_3 carbide during FTS (see ***Figure 2.15*****c-d** and ***Figure 2.16***). Therefore, the *ca.* 360 ppm NMR signal is clearly the signature of a μ_5 carbide.

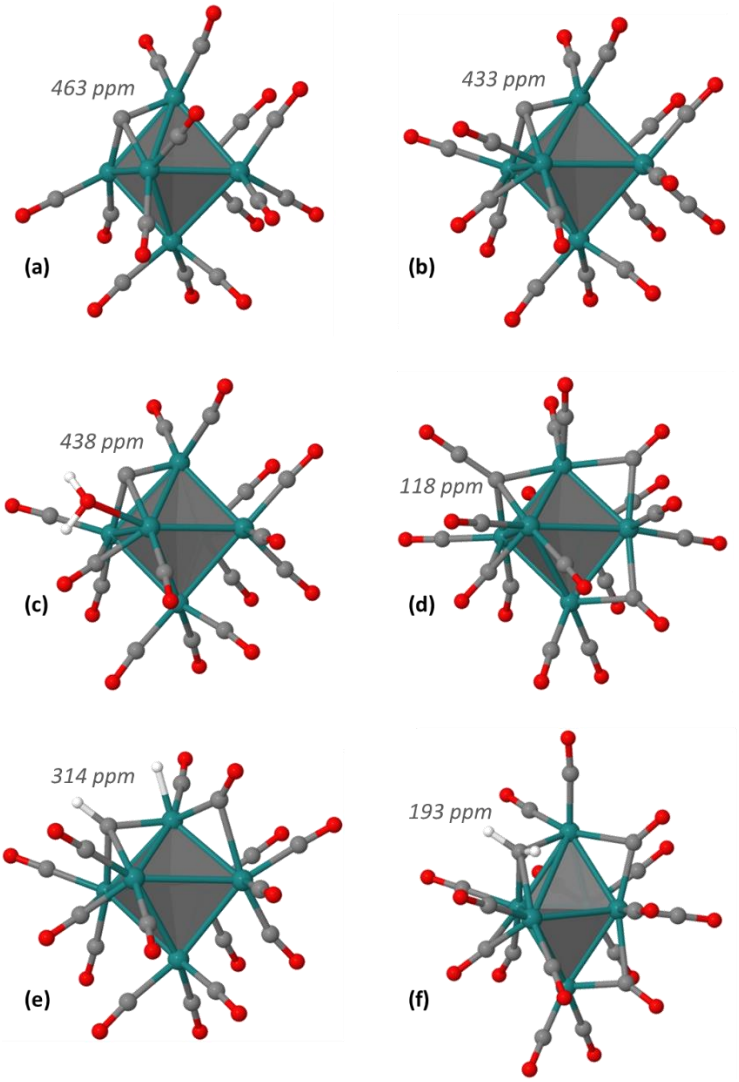

Figure 2.1510. Calculated ^{13}C chemical shifts for the following model clusters: (**a**) [Ru_6]; (**b**) [Ru_6](CO); (**c**) [Ru_6](OH_2); (**d**) [Ru_6](CO)(CCO); (**d**) [Ru_6](CO)(CH)(H); (**f**) [Ru_6](CO)(CH_2).

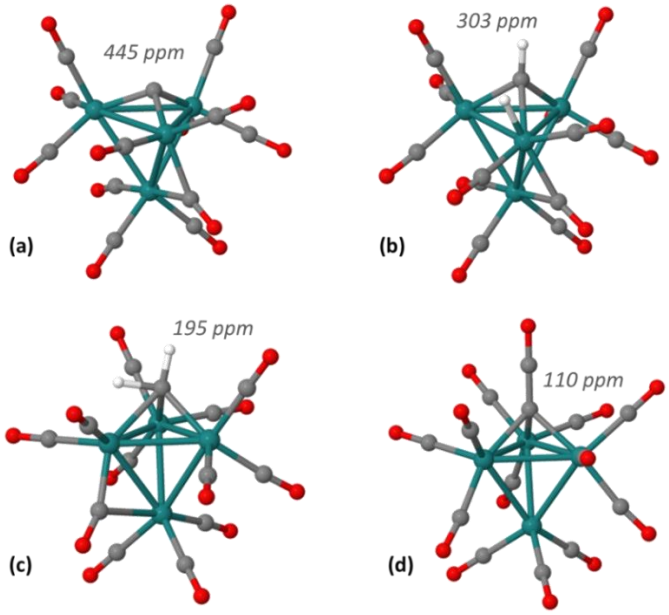

Figure 2.16. Calculated ^{13}C chemical shifts for the following model clusters: (**a**) $[Ru_4](CO)_3$; (**b**) $[Ru_4](CO)_3(CCO)$; (**c**) $[Ru_4](CO)_3(CH)(H)$; (**d**) $[Ru_4](CO)_3(CH_2)$.

Carbides as intermediates in the CO hydrogenation process

Although the current DFT study focuses mainly on the formation of stable carbides on RuNPs, it is attractive to assess the reactivity of such carbide species toward hydrogenation or C-C coupling reactions, as they could be key intermediates in the Fischer-Tropsch synthesis. The relative stabilities of methylene (CH_2*) or ketenylidene (CCO*) intermediates are compared to those of the carbides in which they originate, for several μ_5 and μ_3 carbide species adsorbed at different sites on the Ru_{55} model (*see* ***Figures 2.17*** – ***2.20***). These investigations further emphasize the increased stability μ_5 carbides. The μ_3 carbides, if possibly formed, are most likely merely transient species on the ruthenium surface.

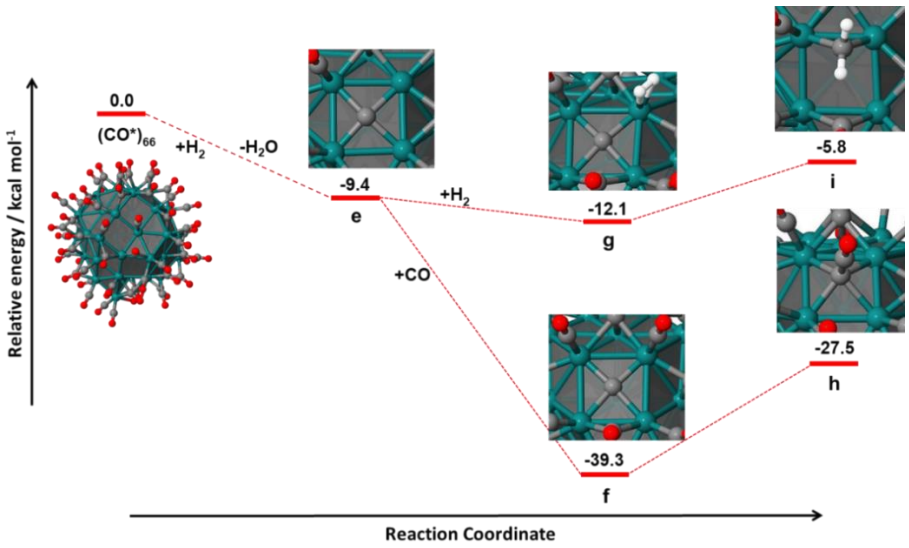

Figure 2.17. Relative DFT energies of several intermediates (**e** – **i**) obtained from a μ_5-carbide by H_2 addition or by C-C couplings, in a four-fold site on the 101 face of the Ru_{55} nanocluster; **e** = $Ru_{66}(CO)^*_{65}C^*$; **f** = $Ru_{66}(CO)^*_{66}C^*$; **g**= $Ru_{66}(CO)^*_{65}C^*(H_2)^*$; **h** = $Ru_{66}(CO)^*_{65}(CCO)^*$; **i** = $Ru_{66}(CO)^*_{65}(CH_2)^*$.

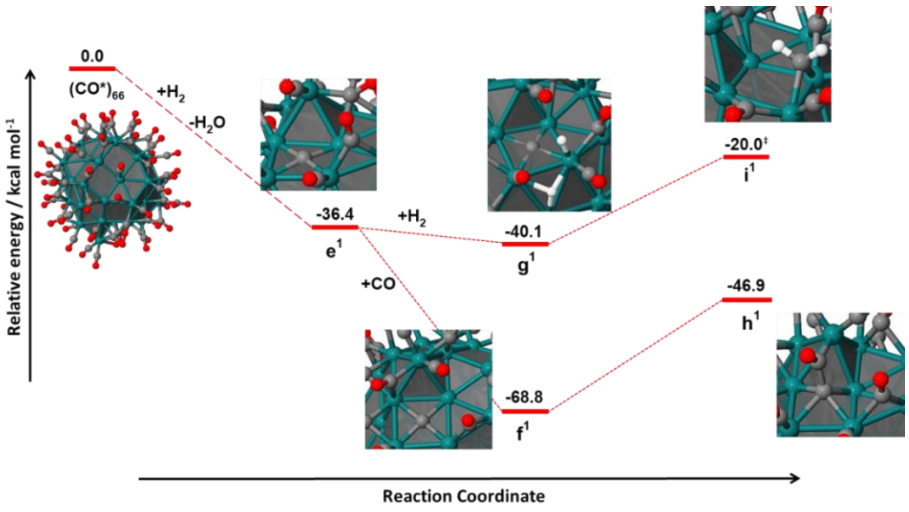

Figure 2.18. Relative DFT energies of several intermediates (**e^1** – **i^1**) obtained from a μ_5-carbide by H_2 addition or by C-C couplings, at the bottom part of the B_5 site; **e^1** = $Ru_{66}(CO)^*_{65}C^*$; **f^1** = $Ru_{66}(CO)^*_{66}C^*$; **g^1** = $Ru_{66}(CO)^*_{65}C^*(H_2)^*$; **h^1** = $Ru_{66}(CO)^*_{65}(CCO)^*$; **i^1** = $Ru_{66}(CO)^*_{65}(CH_2)^*$.

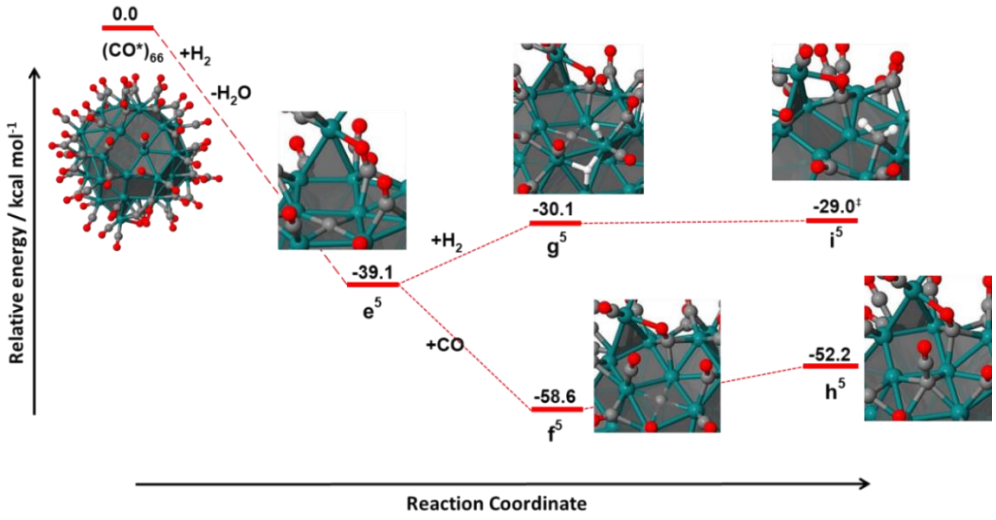

Figure 2.19. Relative DFT energies of several intermediates ($\mathbf{e^5}$ – $\mathbf{i^5}$) obtained from a μ_5-carbide by H_2 addition or by C-C couplings, in a 4-fold site close to a surface complex; $\mathbf{e^5}$ = $Ru_{66}(CO)^*_{65}C^*$; $\mathbf{f^5}$ = $Ru_{66}(CO)^*_{66}C^*$; $\mathbf{g^5}$ = $Ru_{66}(CO)^*_{65}C^*(H_2)^*$; $\mathbf{h^5}$ = $Ru_{66}(CO)^*_{65}(CCO)^*$; $\mathbf{i^5}$ = $Ru_{66}(CO)^*_{65}(CH_2)^*$.

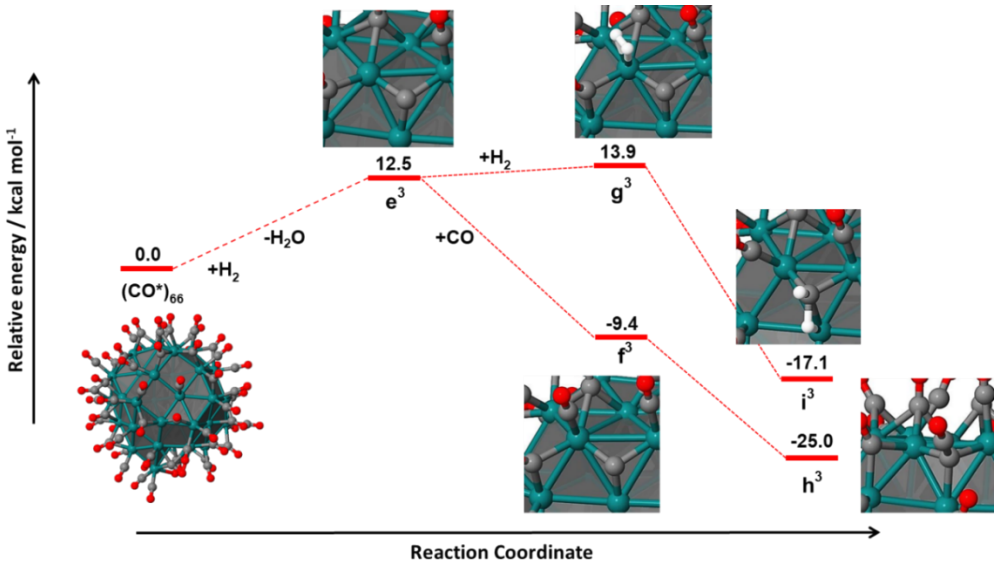

Figure 2.20. Relative DFT energies of several intermediates ($\mathbf{e^3}$ – $\mathbf{i^3}$) obtained from a μ_3-carbide by H_2 addition or by C-C couplings, in a 3-fold site close to a surface complex; $\mathbf{e^3}$ = $Ru_{66}(CO)^*_{65}C^*$; $\mathbf{f^3}$ = $Ru_{66}(CO)^*_{66}C^*$; $\mathbf{g^3}$ = $Ru_{66}(CO)^*_{65}C^*(H_2)^*$; $\mathbf{h^3}$ = $Ru_{66}(CO)^*_{65}(CCO)^*$; $\mathbf{i^3}$ = $Ru_{66}(CO)^*_{65}(CH_2)^*$.

2.3 Brief Summary

Based on extended theoretical mechanistic explorations, coupled with complementary solid-state ^{13}C-NMR studies, DFT-NMR calculations and hydrogen temperature-programmed reduction experiments, the current research emphasized that stable carbides are obtained under relatively mild conditions in standard sites on the surfaces of ultra-small RuNPs, during the CO hydrogenation process.

The results presented in this chapter were disseminated through the publication of a scientific article:

A combined theoretical/experimental study highlighting the formation of carbides on Ru nanoparticles during CO hydrogenation

I.-T. Moraru*, L. M. Martínez-Prieto*, Y. Coppel, B. Chaudret, L. Cusinato, I. del Rosal and R. Poteau*, *Nanoscale*, 2021, **13**, 6902–6915.

2.4 Selected References

(1) L. Cusinato, I. del Rosal and R. Poteau, *Dalton Trans.*, 2017, **46**, 378.

(2) Z. W. Seh, J. Kibsgaard, C. F. Dickens, I Chorkendorff, J. K. Nørskov and T. F. Jaramillo, *Science*, 2017, **355**, 146.

(3) J. A. Trindell, Z. Duan, G. Henkelman and R. M. Crooks, *Chem. Rev.*, 2020, **120**, 814.

(4) T. Wang, X. Cui, K. T. Winther, F. Abild-Pedersen, T. Bligaard and J. K. Nørskov, *ACS Catal*., 2021, **11**, 6290.

(5) B. Hammer and J. K. Nørskov, *Adv. Catal.*, 2000, **45**, 71.

(6) J. K. Nørskov, T. Bligaard, J. Rossmeisl and C. H. Christensen, *Nature Chem.*, 2009, **1**, 37.

(7) I. del Rosal, M. Mercy, I. C. Gerber and R, Poteau*, ACS Nano*, 2013, **7**, 9823.

(8) P. Serp and K. Philippot (Eds), *Nanomaterials in Catalysis*, Wiley-VCH, Weinheim (Germany), **2012**.

(9) K. Philippot and A. Roucoux (Eds), *Nanoparticles in Catalysis: Advances in Synthesis and Applications*, Wiley-VCH, **2021**.

(10) L. M. Martínez-Prieto, S. Carenco, C. H. Wu, E. Bonnefille, S. Axnanda, Z. Liu, P. F. Fazzini, K. Philippot, M. Salmeron and B Chaudret, *ACS Catal*., 2014, **4**, 3160.

(11) W. Chen, T. Lin, Y. Dai, Y. An, F. Yu, L. Zhong, S. Li and Y. Sun, *Catal. Today*, 2018, **311**, 8.

(12) E. Iglesia and D. Hibbitts, *J. Catal.*, 2022, **405**, 614.

(13) R. A. van Santen and A. J. Markvoort, *ChemCatChem*, 2013, **5**, 3384.

(14) I. A. W. Filot, B. Zijlstra, R. J. P. Broos, W. Chen, R. Pestman and E. J. M. Hensen, *Faraday Discuss.*, 2017, **197**, 153.

(15) E. de Smit and B. M. Weckhuysen, *Chem. Soc. Rev*., 2008, **37**, 2758.

(16) K. Xu, B. Sun, J. Lin, W. Wen, Y. Pei, S. Yan, M. Qiao, X. Zhang and B. Zong, *Nat. Commun*., 2014, **5**, 5783.

(17) T. A. Wezendonk, X. Sun, A. I. Dugulan, A. J. F. van Hoof, E. J. M. Hensen, F. Kapteijn and J. Gascon, *J. Catal*., 2018, **362**, 106.

(18) R. J. P. Broos, B. Zijlstra, I. A. W. Filot and E. J. M. Hensen, J*. Phys. Chem. C*, 2018, **122**, 9929.

(19) A. Y Khodakov, W. Chu and P. Fongarland, *Chem. Rev*., 2007, **107**, 1692.

(20) J. X. Liu, H. Y. Su, D. P. Sun, B. Y Zhang and W. X. Li, *J. Am. Chem. Soc*., 2013, **135**, 16284.

(21) B. Zijlstra, R. J. P. Broos, W. Chen, G. L. Bezemer, I. A. W. Filot and E. J. M. Hensen, *ACS Catal*., 2020, **10**, 9376.

(22) R. Zhang, L. Kang, H. Liu, B. Wang, D. Li and M. Fan, *Appl. Catal. B: Environ*., 2020, **269**, 118847.

(23) X.-Y. Quek, I. A. W. Filot, R. Pestman, R. A. van Santen, V. Petkov and E. J. M. Hensen, *Chem. Commun*., 2014, **50**, 6005.

(24) J. Kang, S. Zhang, Q. Zhang and Y. Wang, *Angew. Chem., Int. Ed*., 2009, **48**, 2565.

(25) I. A. W. Filot, R. A. van Santen and E. J. M. Hensen, *Catal. Sci. Technol*., 2014, **4**, 3129.

(26) L. Foppa, C. Copéret and A. Comas-Vives, *J. Am. Chem. Soc*., 2016, **138**, 16655.

(27) L. Foppa, M. Iannuzzi, C. Copéret and A. Comas-Vives, *ACS Catal*., 2018, **8**, 6983.

(28) L. Foppa, M.Iannuzzi, C. Copéret and A. Comas-Vives, *ACS Catal.*, 2019, **9**, 6571.

(29) M. R. Axet and K. Philippot, *Chem. Rev.*, 2020, **120**, 1085.

(30) F. Anya and D. Resasco, *ACS Catal*., 2020, **10**, 4433.

(31) S. Shetty, A. P. J. Jansen and R. A. van Santen, *J. Am. Chem. Soc*., 2009, **131**, 12874.

(32) S. Shetty and R. A. van Santen, *Catal. Today*, 2011, **171**, 168.

(33) P. Zhao, Y. He, D.-B. Cao, H. Xiang, H. Jiao, Y. Yang, Y.-W. Li and X.-D. Wen, *J. Phys. Chem. C*, 2019, **123**, 6508.

(34) I. M. Ciobica and R. A. van Santen, *J. Phys. Chem. B*, 2003, **107**, 3808.

(35) L. Cusinato, L. M. Martínez-Prieto, B. Chaudret, I. del Rosal and R. Poteau, *Nanoscale*, 2016, **8**, 10974.

(36) B. T. Loveless, C. Buda, M. Neurock and E. Iglesia, J*. Am. Chem. Soc*., 2013, **135**, 6107.

(37) J. Liu, D. Hibbitts and E. Iglesia, *J. Am. Chem. Soc*., 2017, **139**, 11789.

Chapter 3

Ruthenium nanoparticles decorated with inorganic amine ligands: DFT perspectives.

3.1 Introduction and Literature Data

This short chapter discusses the possibility of decorating ultra-small RuNPs (*ca.* 1 nm in diameter) with inorganic ancillary ligands, such as hexamethyldisilazane (HMDS). Even though organic amines were long known for their protecting capabilities in case of RuNPs,[1] there are still no reported studies concerning the functionalization of Ru nanoclusters with heavier amine analogues.

The surface chemistry of metal nanoparticles (MNPs) continues to be a developing field,[1] given its increased complexity, but also due to the large number of unexploited molecular species that can act as potential capping agents. Ancillary ligands exhibit steric protection for MNPs, but at the same time adsorbed surface species can tailor the catalytic behaviour of MNPs,[2-4] either by increasing their activity and/or selectivity, either displaying poisoning catalytic effects.[5]

The development of new and efficient MNP catalysts, decorated with unexploited ancillary ligands, represents a big challenge for the scientific community working in the field, but a considerable simplification of the practical efforts is obtained when computational chemistry simulations are performed in parallel.[6-13]

The following section presents some preliminary DFT results concerning the rational design of Ru nanocatalysts decorated with HMDS. Although this species has been previously used as capping agent for iron NPs, its impact on the surface chemistry of RuNPs has not been investigated until now.

3.2 Original contributions

DFT explorations are performed on a Ru_{55} nanocluster model, both in the presence and the absence of surface hydrides, and evaluate the adsorption strength of HMDS ligands for several sites on the metal surface. The adsorption energies HMDS are systematically compared with those of other know capping agents, *e.g.* a convenient reference ligand is its organic counterpart di(*t*-butyl)amine (DTBA) (***Figure 3.1***).

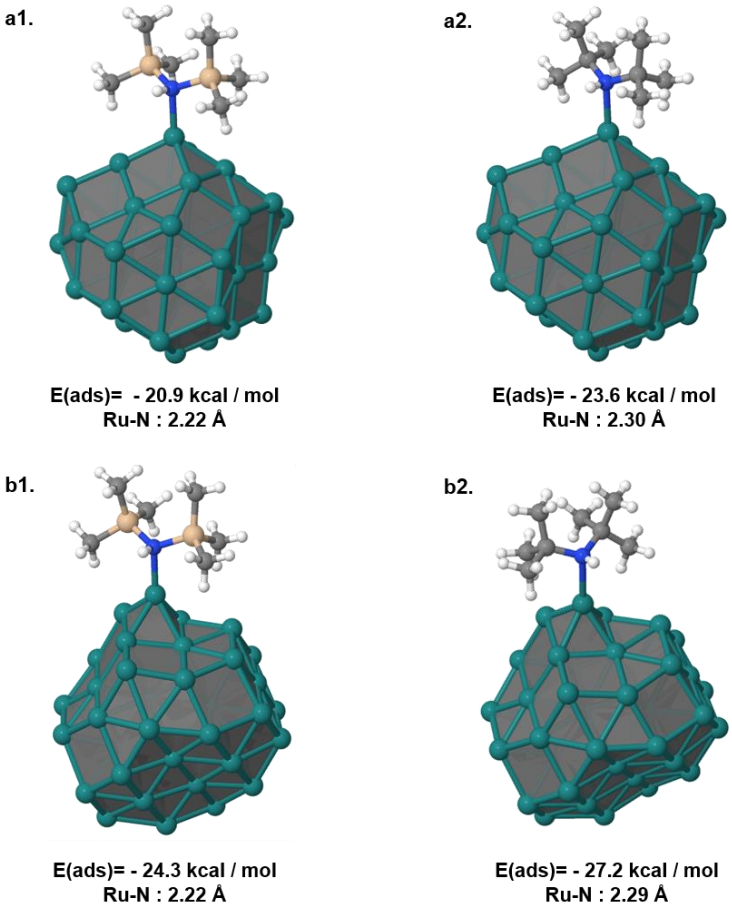

Figure 3.1. Optimized structures of a bare Ru_{55} nanocluster decorated with (**a1**) HMDS - adsorbed at a *corner* atom (*i.e. corner site-1* in ***Table 3.1***); (**b1**) DTBA - adsorbed at the same *corner* atom; (**a2**) HMDS - adsorbed at the tip-ruthenium site (*i.e. tip atom* in ***Table 3.1***); (**b2**) DTBA - adsorbed at the same tip site.

Adsorption energies of DTBA are slightly higher (with *ca.* 3 kcal mol^{-1}) in absolute values than the ones of HMDS. This is quite surprising, as the Ru-N bonds are shorter in the HMDS-decorated RuNP model (see ***Figure 3.1***). A possible explanation for these apparent contradictions is related (at least to some extent) to the energy consumed by these inorganic molecules to significantly alter their geometries by coordination to the ruthenium surface.

The adsorption energy of HMDS is evaluated for several other sites at the surface of the bare Ru_{55} model nanocluster, including corners, edges, or faces (**Table 3.*1***). As a general trend, the adsorption strength is higher for corners than for edge sites and becomes considerably weak on flat terraces.

Table 3.1. Adsorption energies computed for the HMDS ligand at multiple sites on the surface of the bare Ru_{55} nanocluster. Equilibrium Ru-N distances for adsorbed HMDS surface ligands are also displayed. Since several possibilities have been considered for corners and edges, such sites were labelled as *site-1*, *site-2* and so on, so that they could be differentiated.

Type of adsorption site	**Adsorption energy (kcal mol^{-1})**	**Ru-N bond length (Å)**
tip atom	-24.3	**2.22**
corner – site 1	-20.8	**2.22**
corner – site 2	-21.5	**2.23**
corner – site 3	-19.9	**2.24**
corner – site 4	-19.6	**2.25**
edge – site 1	-14.5	**2.27**
edge – site 2	-10.3	**2.33**
flat terrace	-5.6	**2.52**

Next, the adsorption energy of HMDS is calculated for several sites at the surface of a $Ru_{55}H^*_{52}$ NP model (***Figure 3.2***), which is more realistic than the bare Ru_{55} nanocluster (*e.g.* RuNPs

synthesized through the organometallic routes exhibit certain amounts of surface hydrides). It is shown that HMDS adsorption on the $Ru_{55}H^*_{52}$ model is in all cases with 7-8 kcal mol^{-1} weaker compared to its adsorption on the bare NP, but this was to be expected.

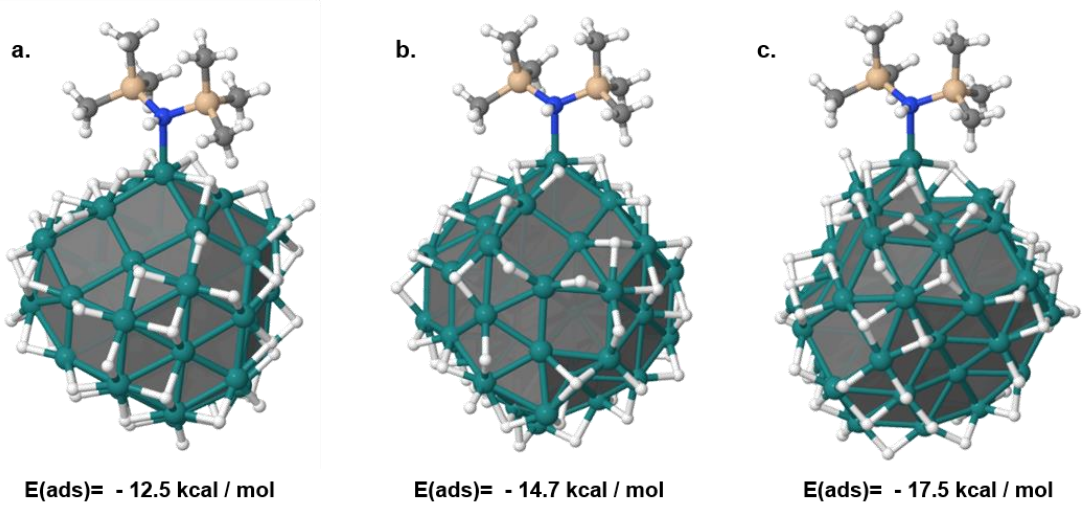

Figure 3.2. Optimized structures of three $Ru_{55}H^*_{52}(HMDS)^*$ nanocluster models, with HMDS coordinated in different adsorption sites on the ruthenium surface: (**a**) corner site - 1; (**b**) corner site - 2; (**c**) tip atom site. Calculated adsorption energies for HMDS are also illustrated

In an even more realistic approach, aiming to reproduce as close as possible the surface composition of actual RuNPs, the coordination at the ruthenium surface of several HMDS ligands is evaluated, both on the bare nanocluster and in the presence of surface hydrides (***Figure 3.3***). For the $Ru_{55}(HMDS)^*_7$ NP model, the average adsorption energy of HMDS is *ca.* -18 kcal mol^{-1}, but becomes considerably lower (in absolute values) in case of the $Ru_{55}H^*_{52}(HMDS)^*_7$ nanocluster.

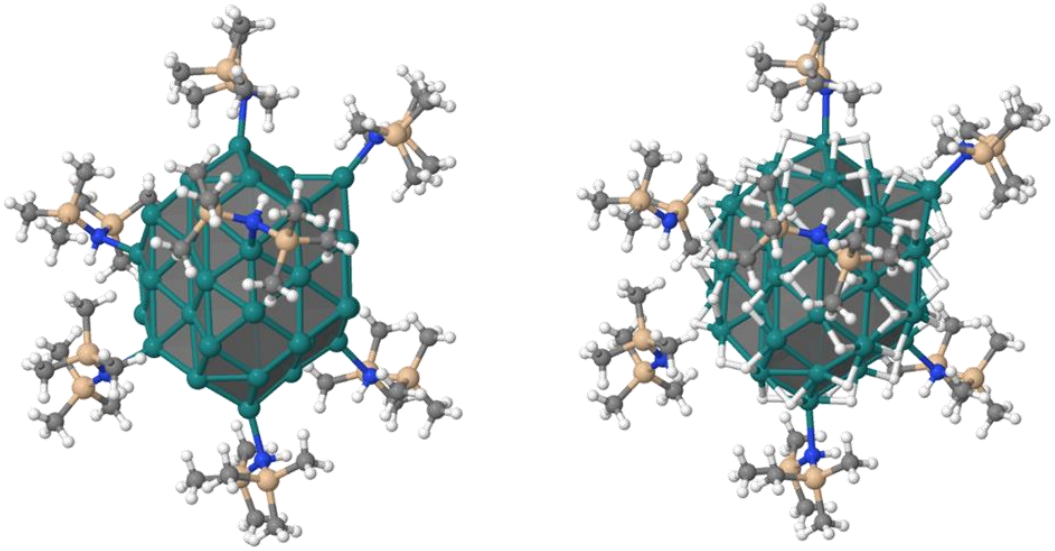

Figure 3.3. Optimized structures of $Ru_{55}H^*_{52}(HMDS)^*_7$ (*left*) and $Ru_{55}H^*_{52}(HMDS)^*_7$ (*right*) NP models. Average adsorption energies for HMDS ancillary ligand are depicted

A possible explanation for the poor adsorption of HMDS in case of the $Ru_{55}H^*_{52}(HMDS)^*_7$ NP is that the current model overestimates the real HMDS/Ru(surface atom) ratio. Therefore, RuNPs decorated with fewer HMDS ligands should be further considered, as well as models involving smaller amounts of co-adsorbed H* species. To establish the exact ratio between adsorbed HMDS* and H* species, *ab-initio* thermodynamic calculations are required. These issues will be addressed in the future stages of this ongoing DFT investigation.

3.3 Brief Summary

The possible functionalization of several Ru_{55} model NPs is investigated by DFT calculations. The relatively low binding energies of HMDS compared to those of known capping agents, *e.g.* NHC ligands or phosphines, correlated with increased volume of this ligand could tailor the surface properties of ultra-small RuNPs. Ruthenium nanoclusters decorated with HMDS ancillary ligands are expected to exhibit high amounts of surface hydrides and, therefore, prospects for increased efficiencies in several catalytic transformations, such as the hydrogenation reactions, or the hydrogen evolution.

3.4 Selected References

(1) L. M. Martínez-Prieto and B. Chaudret, *Acc. Chem. Res*., 2018, **51**, 376.

(2) S. Kunz, *Top. Catal*., 2016, **59**, 1671.

(3) P. Lara and L. M. Martínez-Prieto, *Catalysts*, 2021, **11**, 1210.

(4) A. García-Zaragoza, C. Cerezo-Navarrete, A. Mollar-Cuni, P. Oña-Burgos, J. A. Mata, A. Corma and L. M. Martínez-Prieto, *Catal. Sci. Technol*., 2022, **12**, 1257.

(5) E. Bonnefille, F. Novio, T. Gutmann, R. Poteau, P. Lecante, J.-C. Jumas, K. Philippot and B. Chaudret, *Nanoscale*, 2014, **6**, 9806.

(6) L. Cusinato, I. del Rosal and R. Poteau, *Dalton Trans.*, 2017, **46**, 378.

(7) Z. W. Seh, J. Kibsgaard, C. F. Dickens, I Chorkendorff, J. K. Nørskov and T. F. Jaramillo, *Science*, 2017, **355**, 146.

(8) J. A. Trindell, Z. Duan, G. Henkelman and R. M. Crooks, *Chem. Rev.*, 2020, **120**, 814.

(9) T. Wang, X. Cui, K. T. Winther, F. Abild-Pedersen, T. Bligaard and J. K. Nørskov, *ACS Catal*., 2021, **11**, 6290.

(10) B. Hammer and J. K. Nørskov, *Adv. Catal.*, 2000, **45**, 71.

(11) J. K. Nørskov, T. Bligaard, J. Rossmeisl and C. H. Christensen, *Nature Chem.*, 2009, **1**, 37.

(12) I. del Rosal, M. Mercy, I. C. Gerber and R, Poteau*, ACS Nano*, 2013, **7**, 9823.

(13) M. A. Ortuño and Núria López, *Catal. Sci. Technol*., 2019, **9**, 5173.

General Conclusions

The thesis entitled *"From molecular inorganic species to organometallic nanoparticles: a DFT journey"* is based on two research directions. The first one is related to the molecular chemistry of both organic and inorganic counterparts of amines and ethers (*Chapter 1*), focusing on their chemical bonding, while the second topic concerns the surface chemistry of ultra-small ruthenium nanoparticles (*Chapter 2*), special attention being paid to the formation of carbides during CO hydrogenation. By crossing the knowledge of these two themes, it resulted a third chapter, aiming at decorating ruthenium nanoclusters with silylamine ligands.

The first chapter consists of a comprehensive computational chemistry investigation that addressed some fundamental issues related to the nature of the chemical bond in both organic and inorganic counterparts of amines and ethers. By analysing a wide range of molecular systems that incorporate the E-O-E or E_3N fragment (E = C, Si, Ge, Sn), the present study developed a general bonding model that fills some gaps of previously reported approaches. This model accounts for the counterbalance between attractive [LP(Y)→σ*(E-X) hyperconjugations, LP(Y)→d(E) donations] and repulsive [LP(Y)···σ(E-X) Pauli repulsions] interactions (Y = O or N; X = H, C, O, F or Cl), to describe deviations from an ideal covalent bond picture. Maximization of the energy offset between attractions and repulsions for heavier ether/amine homologues explains not only their specific geometries, but also the contrasting structural features between organic and inorganic counterparts. Another important result of the current research is related to the participation of LP(Y)→d(E) (Y = O or N) interactions into the bonding mechanism of these inorganic derivatives, although such effects have lately been regarded as computational chemistry artefacts derived from the polarization functions of the basis sets. It was also shown that the two lone pair electrons at the oxygen atom of E-O-E systems affect the molecular geometries of these species in different manners: the attraction-repulsion offsets originating in s/p LP dictate the bending behaviour of the E-O-E units, while those generated by the pure p LP influence the equilibrium distances of E-O bonds.

The results presented in the second chapter shed further light on the existence of stable surface carbides on ultra-small and pure RuNPs. Based on an extensive DFT mechanistic investigation, carried out on a Ru_{55} model NP that is realistic in size, structure and surface composition, the current research has highlighted that μ_5 ruthenium carbides are exothermically formed in the presence of water via hydrogen-assisted hydroxymethylidyne mechanisms. These reactions occur at reasonable kinetic cost, in any available standard four-fold site at the surface of Ru NPs and not only in steps as indicated by previous studies. On the other hand, the possible formation of μ_3 carbides is endothermic and involves higher barriers. The current theoretical findings have been confirmed by solid-state ^{13}C-NMR explorations, resulting from a collaboration with an experimental group in Toulouse. DFT-NMR calculations secured the assignment of the experimental NMR data, stressing that the *ca.* 360 ppm resonance signal corresponds to a μ_5 carbide and not to a μ_3 one, nor to other possible intermediates formed during the CO hydrogenation process. Other interesting side results of the mechanistic study suggest the formation of stable μ_6 carbides, species that have never been reported for Ru NPs until now but are common for ruthenium molecular clusters, as well as a peculiar but very stable surface pseudo-octahedral ruthenium complex that exhibits a μ-Ru atom binding the remaining Ru_{54} moiety.

The last chapter discussed the possible functionalization of ruthenium nanoclusters with silylamine ligands. These DFT data are preliminary, but so far are encouraging, with prospects for designing RuNPs decorated with hexamethyldisilazane (HMDS) ligands that exhibit tailored surface properties. The increased bulkiness of the unexploited HMDS ligand with respect to commonly employed capping agents, such as organic amines or alcohols, could provide, on one hand, better steric protection for RuNPs. On the other hand, the relatively low adsorption strength of HMDS compared to that of NHC species, or phosphine ligands, should allow its reversible adsorption to the surface, as well as an increased amount of co-adsorbed hydrides for RuNPs synthesized via the organometallic route. Therefore, ultra-small RuNPs decorated with HMDS ligands could benefit from increased catalytic efficiencies in hydrogenation processes or the hydrogen evolution reaction.

List of Publications

Scientific articles related to the thesis topic

1. *Offsets between Hyperconjugations, p→d Donations and Pauli Repulsions Impact the Bonding of E–O–E Systems. Case study on Elements of Group 14*
   I.-T. Moraru*, F. Teleanu, L. Silaghi-Dumitrescu and G Nemes*, *Phys. Chem. Chem. Phys.,* 2022, **24**, 13217. (**IF:** 3.945)

2. *A Combined Theoretical/Experimental Study Highlighting the Formation of Carbides on Ru Nanoparticles during CO Hydrogenation*
   I.-T. Moraru*, L. M. Martínez-Prieto*, Y. Coppel, B. Chaudret, L. Cusinato, I. del Rosal and R. Poteau*, *Nanoscale*, 2021, **13**, 6902. (**IF:** 8.307)

3. *Theoretical Insights into the Structural Differences between Organic and Inorganic Amines/Ethers.*
   I.-T. Moraru*, F. Teleanu and G Nemes*, *J. Phys. Chem. A,* 2020, **124**, 8246. (**IF:** 2.944)

4. *Bridging a Knowledge Gap from Siloxanes to Germoxanes and Stannoxanes. A Theoretical Natural Bond Orbital Study*
   I.-T. Moraru, P. M. Petrar and G Nemes *J. Phys. Chem. A*, 2017, **121**, 2515. (**IF:** 2.944)

Scientific articles resulted from side projects

5. *Novel Coordination Compounds Featuring 9-Chloro-9-Phosphaalkenylchloro-9-Germafluorene Ligands*
   N. Deak, R. Septelean, L. Buta, **I.-T. Moraru**, I. A. Cretoiu, A. Soran and G. Nemes, *Polyhedron*, 2022, **221**, 115866. (**IF:** 2.975*)*

6. *Unexpected Helical Supramolecular Assembly of a Simple Achiral Acetamide Tecton Generates Selective Water Channels*
   D. Dumitrescu, J. Rull-Barrull, A. Martin, N. Masquelez, M. Polentarutti, A. Heroux, N. Demitri, G. Biais, **I.-T. Moraru**, R. Poteau, M. Amblard, A. Krajnc, G. Mali, Y.-M. Legrand, A. van der Lee and B. Legrand, *Chem. Eur. J.*, 2022, **28**, e202200383. (**IF:** 5.020)

7. *The Modulation of 9-Chloro-9-Phosphaalkenylchloro-9-Germafluorene Reactivity through Organolithium Reagents*
   L. Buta, R. Septelean, A. Soran, I. A. Aghion, **I.-T. Moraru** and G. Nemes, *Polyhedron*, 2021, **210**, 115505. (**IF:** 2.975)

8. *Solid-State and Theoretical Investigations of Some Banister-Type Macrocycles with 2, 2'-Aldoxime-1, 1'-Biphenyl Units*,
   I. Stroia, **I.-T. Moraru**, M. Miclăuş, I. Grosu, C. Lar, I. G. Grosu and A. Terec, *Front. Chem*., 2021, **9**, 750418. (**IF:** 5.545)

9. *Mo thio and Oxo-thio Molecular Complexes Film as Self-healing Catalyst for Photocatalytic Hydrogen Evolution on 2D Materials*
   J. Barros Barbosa, P. L. Taberna, V. Bourdon, I. C. Gerber, R. Poteau, A. Balocchi, X. Marie, J. Esvan, P. Puech, A. Barnabé, L. Da Gama Fernandes Vieira, **I.-T. Moraru** and J. Y. Chane-Ching, *Appl. Catal. B*, 2020, **278**, 119288. (**IF:** 24.319)

10. *Synthesis and Characterization of a Novel Bis-Sulfoxide and Its Evaluation as a Ligand in p-Block Chemistry*
    N. Deak, O. Thillaye du Boullay, S. Mallet-Ladeira, I.-T. Moraru, D. Madec and G. Nemes, *Eur. J. Inorg. Chem.*, 2020, **2020**, 3729. (**IF:** 2.551)

11. *Oxidation of sp^2 versus sp^3 Phosphorus Atom in 1, 3-Diphosphapropenes. a DFT Study*
    I.-T. Moraru, R. Septelean and G. Nemes, *Rev. Roum. Chim*., 2020, **65**, 747. (**IF:** 0.410)

12. *New Stable 2,3-Dichloro,1,3-Diphosphapropenes; Synthesis and Characterization*
    R. Septelean, A. Muresan, A. Soran, **I.-T. Moraru** and G. Nemes, *Rev. Roum. Chim*., 2020, **65**, 579. (**IF:** 0.410)

13. *New stable 3,1-Germaphosphapropenes. Synthesis and Structural Characterization*
    L. Buta, R. Septelean, **I.-T. Moraru**, A. Soran, L. Silaghi-Dumitrescu and G. Nemes, *Inorg. Chim. Acta*, 2019, **486**, 648. (**IF:** 3.118)

14. *A Non-Symmetric Sulfur-Based O,C,O-Chelating Pincer Ligand Leading to Chiral Germylene and Stannylene*
    N. Deak, O. T. du Boullay, **I.-T. Moraru**, S. Mallet-Ladeira, D. Madec and G. Nemes, *Dalton Trans*., 2019, **48**, 2399. (**IF:** 4.569)

15. *A DFT Investigation of a Polycyclic Stannylene Model; Structural Characterization and Stability Assessment*
    I.-T. Moraru and G. Nemes, *Studia UBB Chemia*, 2019, **64**, 435. (**IF:** 0.558)

16. *Palladium and Ruthenium Derivatives Stabilised by Bis-sulfone Ligand*
    N. Deak, R. Septelean, **I.-T. Moraru**, S. Mallet-Ladeira, D. Madec, and G. Nemes, *Studia UBB Chemia*, 2018, **63**, 105. (**IF:** 0.558)

17. *Computational and Experimental Investigation of Phosphaalkenyl Germylenes from Donor-Acceptor Perspective*
    R. Septelean[1], **I.-T. Moraru[1]**, T.-G. Kocsor, N. Deak, N. Saffon-Merceron, A. Castel and G. Nemes, *Inorg. Chim. Acta*, 2018, **475**, 112. (**IF:** 3.118)

18. *Reactivity of Bis(sulfonyl)O,C,O-Chelated Metallylenes in Cycloaddition with ortho-Benzoquinone: an Experimental and Computational Study*
    N. Deak, **I.-T. Moraru**, N. Saffon-Merceron, D. Madec and G. Nemes, *Eur. J. Inorg. Chem*., 2017, **2017**, 4214. (**IF:** 2.551)

19. *Residential, Soil and Water Radon Surveys in North-Western Part of Romania*
    A. Cucoş (Dinu), B. Papp, T. Dicu, M. Moldovan, D. B. Burghele, **I.-T. Moraru**, A. Tenţer and C. Cosma, *J. Environ. Radioact*., 2017, **166**, 412. (**IF:** 2.655)

Conference presentations

Oral Presentations

1. *Evaluating the Aromatic Character of Benzene-like Inorganic Compounds by Means of Theoretical Calculations*
   A.-C. Tomuț, **I.-T. Moraru**, *XVIII International Conference Students for Students*, **6-10 April 2022**, Cluj-Napoca, **Romania**

2. *Oligomers of Inorganic Ethers. A DFT Study*
   F. Teleanu, **I.-T. Moraru**, G. Nemes, *XVI International Conference Students for Students*, **2-6 April 2019**, Cluj-Napoca, Romania.

3. *On the Possible Presence of Carbides in the Fischer-Tropsch Process Catalyzed by Ruthenium Nanoparticles: a DFT Study*
   I.-T. Moraru, L. M. Martínez-Prieto, B. Chaudret, I. del Rosal, R. Poteau, *Molecular Modelling in Chemistry and Biochemistry- MOLMOD*, **28-30 October 2018**, Cluj-Napoca, Romania.

4. *Towards a Comprehensive Overview of E-O and E-N Chemical Bondings (E = Si, Ge, Sn) in Neutral and Cationic Species; a DFT Case Study*
   I.-T. Moraru, F. Teleanu, G. Nemes, *A XXXV-a Conferinţă Naţională de Chimie*, **2-5 October 2018**, Calimăneşti-Căciulata, Romania.

5. *Relația dintre Hiperconjugare şi Planaritate – Un Studiu DFT al Aminelor Anorganice şi Compușilor Izoelectronici*
   F. Teleanu, **I.-T. Moraru**, G. Nemes, *Sesiunea de Comunicări Ştiinţifice a Studenţilor, Masteranzilor şi Doctoranzilor*, **29-30 June 2018**, Iaşi, Romania.

6. *A Theoretical Investigation of Electronic Interactions in Inorganic Amines and Isoelectronic Compounds with Silicon, Germanium and Tin*
   F. Teleanu, **I.-T. Moraru**, G. Nemes, *Sesiunea de Comunicări Ştiinţifice Studenţesti*, **25-26 May 2018**, Bucureşti, Romania.

7. *A DFT Study Concerning the Structural Features of Amines' and Ethers' Heavier Analogues with Silicon, Germanium and Tin*
   F. Teleanu, **I.-T. Moraru**, G. Nemes, *XV International Conference Students for Students*, **18-22 April 2018**, Cluj-Napoca, Romania.

8. *Theoretical Modeling of the Fischer-Tropsch Synthesis Catalyzed by Small Ruthenium Nanoparticles: First Steps*
   L. Cusinato, **I.-T. Moraru**, L. M. Martínez-Prieto, B. Chaudret, I. del Rosal, R. Poteau, *Molecular Modelling in Chemistry and Biochemistry- MOLMOD*, **13-15 November 2016**, Cluj-Napoca, Romania.

9. *Investigating the Structure of Siloxanic, Germoxanic and Stannoxanic Species. A NBO Approach*
   I.-T. Moraru, P. M. Petrar, G. Nemeş, *Molecular Modelling in Chemistry and Biochemistry- MOLMOD*, **13-15 November 2016**, Cluj-Napoca, Romania.

10. *Understanding the Structure of Siloxanic, Germoxanic and Stannoxanic Species*
    I.-T. Moraru, G. Nemeş, *MatCatNet Conference "From Molecules to Functionalised Materials"*, **3-5 September 2016**, Ohrid, North Macedonia.

11. *Assessing Chemical Bonding in Disiloxanic, Digermoxanic and Distannoxanic Species*
    I.-T. Moraru, P. M. Petrar, G. Nemes, *Young Researchers' Interactional Conference on Chemistry and Chemical Engineering*, **12–14 May 2016**, Cluj-Napoca, Romania.

12. *Hyperconjugative Interactions within Trisiloxanic, Trigermoxanic and Tristannoxanic Derivatives*
    I.-T. Moraru, P. M. Petrar, G. Nemes, *XIIIth International Conference Students for Students*, **13-17 April 2016**, Cluj-Napoca, Romania.

13. *Rationalizing the Structural Behaviour of Some Oxanes Containing Group 14 Elements Using Theoretical Calculations*
    I.-T. Moraru, P. M. Petrar, *MatCatNet Conference "From Molecules to Functionalised Materials"*, **17-21 September 2015**, Ohrid, North Macedonia.

Poster Presentations

1. *Towards a Unitary Description of E-O and E-N Bonds (E = SI, Ge, Sn); from Inorganic Ethers to Amines and Isoelectronic Species*
   I.-T. Moraru, F. Teleanu, G. Nemes, *Molecular Modelling in Chemistry and Biochemistry - MOLMOD*, **28-30 October 2018**, Cluj-Napoca, Romania.

2. *Correlations between Number of Electrons and Structural Features of Neutral and Ionic $(ER_3)_3Z$ Species (E = B, C; E = Si, Ge, Sn; R = H, Me)*
   F. Teleanu, **I.-T. Moraru**, G. Nemes, *The XXXV-th National Chemistry Conference*, **2-5 October 2018**, Calimăneşti-Căciulata, Romania.

3. *Assessment of the E-O, E-N and E-B Chemical Bonding (E = Si, Ge, Sn) in Neutral and Cationic Derivatives*
   I.-T. Moraru, F. Teleanu, R. Septelean, G. Nemes, *Young Researchers' Interactional Conference on Chemistry and Chemical Engineering*, **3–5 May 2018**, Budapest, Hungary.

4. *New Insights Regarding Chemical Bonding within Heavier Analogues of Ethers: Siloxanes, Germoxanes and Stannoxanes*
   I.-T. Moraru, G. Nemes, *11th Triennial Congress of the World Association of Theoretical and Computational Chemists (WATOC)*, **27 August – 1 September 2017**, München, Germany.

5. *Towards New Germaphosphaalkenyl Derivatives*
   L. Buta, **I.-T. Moraru**, G. Nemes, L. Silaghi-Dumitrescu, *European Workshop on Phosphorus Chemistry - EWPC 14/2017*, **20-22 March 2017**, Cluj-Napoca, Romania.

6. *A Comprehensive NBO Study Regarding the Bond Formation in Siloxanes, Germoxanes and Stannoxanes*
   I.-T. Moraru, G. Nemeş, *A XXXIV-a Conferinţă Naţională de Chimie*, **4-7 October 2016**, Calimăneşti-Căciulata, Romania.

7. *Discussing the Nature of the Chemical Bonding in Group 14 Acyclic Oxanes through DFT Calculations*
   I.-T. Moraru, P. M. Petrar, *XIIth International Conference Students for Students*, **22-26 April 2015**, Cluj-Napoca, Romania.

8. *Assessment of Structural Features of Acyclic Stannasiloxaic Compounds through DFT Calculations*
   I.-T. Moraru, P. M. Petrar, *Molecular Modelling in Chemistry and Biochemistry - MOLMOD*, **13-15 November 2014**, Cluj-Napoca, Romania.